Aggregate

WILEY

Aggregate Open Access

REVIEW OPEN ACCESS

Excited State Structure and Decay Rates for Aggregates

Zhigang Shuai[1,2] | Qi Sun[2,3] | Jiajun Ren[2,4] | Tong Jiang[2,5] | Weitang Li[1,2]

[1]School of Science and Engineering, The Chinese University of Hong Kong, Shenzhen, China | [2]Department of Chemistry, MOE Key Laboratory for Organic OptoElectronics and Molecular Engineering, Tsinghua University, Beijing, China | [3]Department of Chemistry and Biochemistry, University of Arizona, Tucson, Arizona, USA | [4]Key Laboratory of Theoretical and Computational Photochemistry, Ministry of Education, College of Chemistry, Beijing Normal University, Beijing, China | [5]Department of Chemistry and Chemical Biology, Harvard University, Cambridge, Massachusetts, USA

Correspondence: Zhigang Shuai (shuaizhigang@cuhk.edu.cn)

Received: 24 December 2024 | **Revised:** 23 January 2025 | **Accepted:** 23 January 2025

Funding: This work was supported by the National Natural Science Foundation of China (grant nos. T2350009 and 22433007), the Guangdong Provincial Natural Science Foundation (grant no. 2024A1515011185), the Shenzhen City Pengcheng Peacock Talent Program, and Shenzhen Science and Technology Program (no. KQTD20240729102028011). Jiajun Ren is supported by the National Natural Science Foundation of China (grant nos. 22273005 and 22422301).

Keywords: charge transfer | electron-vibration coupling | excited state | molecular aggregate

ABSTRACT

Electronic excited state in molecular aggregate or exciton states continue to attract great attention due to the increasing demands for applications of molecular optoelectronics and sensing technology. The working principle behind the application is closely related to the excited state structure and dynamic processes in molecular aggregate. In our previous review article (Aggregate 2021; 2: e91), we focused more on the molecular mechanism for aggregation-induced emission process. Here, we are going to summarize our recent progress on theoretical investigations on the effects of excitonic coupling (J) and the intermolecular charge transfer (CT) on the excited state structure and dynamic processes. These are in general missing for molecular quantum chemistry studies. We will first present a novel definition of exciton coherence length which can present a bijective relation with the radiative decay rate and obviously we have clarified the confusion appeared in literature. Then, we will look at the CT effect for aggregate starting from a simple three-state model coupled with quantum chemical calculation for molecular dimer and we focus on the intensity borrowing, which can turn H-aggregate into emissive when the electron transfer and hole transfer integrals possessing the same sign and being large enough. We are able to propose a molecular descriptor to design molecular materials possibly possessing both high photoluminescence quantum yield and carrier mobility. Finally, we introduce our work on the modified energy gap law for non-radiative decay rate in aggregates. We found there exist optimal J to minimize the non-radiative decay loss.

1 | Introduction

The discovery of aggregation-induced emission (AIE) by Tang and coworkers in 2001 [1] has continuously stimulated investigation of molecular aggregation effect. Exotic phenomena such as non-conjugated cluster luminescence, pure organic room temperature phosphorescence, aggregation-modified circularly polarized luminescence, etc., have been reported from quite different chemical systems, including organic, inorganic, metal-coordinated, or biological. In general, from a theoretical perspective, there are three typical approaches to describe materials, namely, at the molecular level, atomic/molecular clusters, and solids with periodicity. Chemists like molecules. Quantum chemistry computational packages represented by the Gaussian series have gained tremendous influence, while condensed matter physicists prefer solids, employing widely Vienna Ab initio Simulation Package. As far as aggregates are concerned, cluster approach based on molecular quantum chemistry and supercell approach based on solid state physics are commonly practiced. These are mostly for ground state properties. Since most people in the field are interested in optical-related phenomenon, the essential issue is the excited state. The most popular molecular excited state computational method is undoubtedly time-dependent density functional theory, while around 20 years ago, it was semiempirical INDO/S method as implemented in ZINDO package. In this respect, Brédas et al. had played a leading role in revealing the nature of intermolecular interaction for excited state through cluster model [2]. From solid state physics, band structure theory works predominantly for most of materials with small exciton binding energy. To go beyond such one particle picture, GW plus Bethe–Salpeter equation (BSE) have achieved great success, namely, GW describes electron or hole quasi-particle band, while BSE gives exciton band. Exciton contains the attraction between electron and hole. In molecular and polymeric materials, exciton dominates the optical processes. The latter is governed not onlyby electronic structure, but also by dynamics. For condensed phases, very often, the dynamical processes are determined by electron–phonon coupling since the environment restricts molecules from drastic motions such as bond breaking or formation. As far as optical emission and absorption are concerned and if the photochemical reaction is not involved, Kasha's aggregate model forms the foundation of exciton band model, where only intermolecular transition dipole coupling is considered [3]. Then, we had the Frenkel–Holstein model where only intramolecular vibration is considered. In addition, intermolecular charge transfer (ICT) and intermolecular vibrational coupling could also play important roles. The latter is often coined as Peierls term such as the popular Su-Schrieffer–Heeger model [4]. Intramolecular vibration charge transfer (CT), and intermolecular vibration can demonstrate different effects on the optical excitation or emission processes. For example, Spano carefully examined the nature of CT state in aggregates and its effect on the excited state ordering. He found that CT can turn H-type aggregate to J-type or vice versa [5, 6]. Through quantum mechanics/molecular mechanics (QM/MM) computational study, we found similar phenomena but with different microscopic origins, namely, aggregates could turn dark n-π^* transition to bright π–π^*, even without any ICT [7]. Recently, Fratini et al. found that the intermolecular vibrational coupling plays a leading role and suggested transient localization picture for both charge transport and exciton migration [8], which presented completely different behavior from the conventional Marcus theory.

The complicated nature of the interactions posed great challenges for theoretical descriptions of molecular aggregates in both excited state electronic structure and dynamical processes. Our group started to look at the AIE from molecular excited state vibrational relaxation rate processes with and without surroundings so that we can identify how surrounding molecules suppress vibrational relaxation and render a quantitative description for AIE. In fact, the molecular approach to AIE can be justified by the fact that for quite some AIEgens, the ratio of intermolecular excitonic coupling with respect to intramolecular reorganization energy λ is always less than 0.17 [9]. The effect of J on the excited state radiative and non-radiative decay is of great challenge and in this review article, we are going to present some of our recent work. First, we will present a unified definition of exciton coherence length (ECL) with bijective correlation with radiative decay rate. Then, we presented a quantum chemistry calculation for molecular dimer to analyze the intensity borrowing effect for CT state and we derived molecular descriptors as to turn the dark state of H-type into bright. In fact, for carrier transport, H-aggregate is more favorable than J-aggregate. Thus, our strategy provided an efficient way to design highly luminescent materials with high carrier mobility. And it indeed works because chemists have successfully synthesized the compound with targeted property. Last, we will present a perturbative formalism to calculate the non-radiative decay rate k_{nr} for molecular aggregate based on time-dependent density matrix renormalization group (TD-DMRG) theory. We found there exists optimal excitonic coupling to minimize k_{nr}.

2 | Exciton Coherence

2.1 | Kasha's Theory

Starting from the simplest dimer model made of two identical chromophores, Kasha's model [10] has been used to understand the photophysical properties of a large class of molecular aggregates. Upon photo-excitation, a single molecule absorbs a photon at a certain wavelength, and experiences an ($S_0 \rightarrow S_1$) electronic transition from the ground state to its excited state, $|g_1\rangle \rightarrow |e_1\rangle$. There are four possible states for the dimer model: $|g_1g_2\rangle$, $|g_1e_2\rangle$, $|e_1g_2\rangle$, and $|e_1e_2\rangle$. The double-excitation state $|e_1e_2\rangle$ is typically much higher in energy than the single-excitation states $|g_1e_2\rangle$ and $|e_1g_2\rangle$. In many cases, the dynamics of interest, such as exciton or energy transfer, primarily involve single-excitation states [11–14]. With weak interactions, non-radiative energy transfer between the localized chromophores (e.g., in fluorescent proteins) [15, 16] occurs via Förster resonance energy transfer (FRET) [17]. FRET is short-ranged and resonant because the donor emission energy closely matches the acceptors absorption energy, with efficiency decaying as with a $1/r^6$ dependence [14]. In contrast, strong dipole–dipole coupling with a long-range $1/r^3$ dependence, delocalizes excitations across multiple chromophores, forming delocalized exciton states. This review focuses on systems with strong interactions that create these delocalized excitations. In this section, we focus on the exciton structure when the intermolecular distance is relatively large such that the long-ranged Coulomb interactions dominate the electronic couplings. In Section 3, we will also delve into cases where the intermolecular distance is short enough which makes CT interactions not negligible [5].

Kasha's model constructed a 2 × 2 Hamiltonian defined on the basis of the single-excitation states, $|g_1e_2\rangle$ and $|e_1g_2\rangle$:

$$\hat{H} = \begin{pmatrix} E_{\mathrm{ex}} & J \\ J & E_{\mathrm{ex}} \end{pmatrix} \tag{1}$$

where E_{ex} is the excitation energy of the monomer and J is the Coulomb exciton coupling between the two chromophores, which can be obtained by different approximations [18–20] or by more accurate quantum chemical calculations [21–24]. We show the schematic representation of the Kasha's model in Figure 1, where the eigenstates amount to a bright state $|+\rangle$ and a dark state $|-\rangle$:

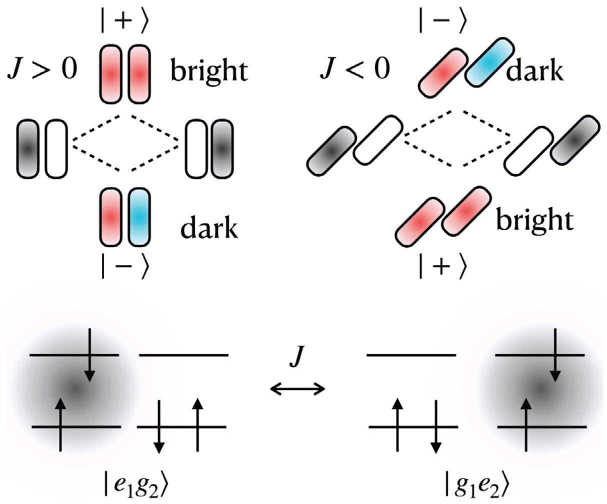

FIGURE 1 | Schematic representation of Kasha's model for a dimer system. Different colors represent different phases of the wave functions.

$$|+\rangle = \frac{1}{\sqrt{2}}\left(|g_1e_2\rangle + |e_1g_2\rangle\right),\ |\langle\hat{\mu}\rangle|^2 = 2\mu^2 \tag{2}$$

$$|-\rangle = \frac{1}{\sqrt{2}}\left(|g_1e_2\rangle - |e_1g_2\rangle\right),\ |\langle\hat{\mu}\rangle|^2 = 0 \tag{3}$$

where $\hat{\mu}$ is the dipole operator and μ is the transition dipole moment of a single molecule. The energy of the bright state is $E_{\text{ex}} + J$, and the energy of the dark state is $E_{\text{ex}} - J$. The bright state is optically active and has doubled oscillator strength compared to the monomer, while the dark state is optically forbidden. Depending on the sign of J, the aggregate can be classified as H-aggregate ($J > 0$) or J-aggregate ($J < 0$) [25]. In J-aggregates, the bright state is lower in energy, and since emission occurs from the lowest excited state at zero temperature, the aggregate is emissive. Whereas in H-aggregates, the bright state is higher in energy while the lowest state is dark, and this simple model predicts non-emissive aggregate at zero temperature. The Frenkel exciton model is a generalization of Kasha's model to molecular aggregates composed of N monomers [26],

$$\hat{H} = \sum_{i}^{N} E_i a_i^{\dagger} a_i + \sum_{i,j}^{N} J_{ij} a_i^{\dagger} a_j \tag{4}$$

where E_i is the excitation energy of the ith monomer, and J_{ij} is the exciton coupling between the ith and jth monomers. We have used the creation (excitation) and annihilation (de-excitation) operators $a_i^{\dagger}$ and a_i:

$$|i\rangle = a_i^{\dagger}\,|g\rangle = |\cdots g_{i-1}e_i g_{i+1}\cdots\rangle \tag{5}$$

$$|g\rangle = a_i\,|i\rangle = |\cdots g_{i-1}g_i g_{i+1}\cdots\rangle \tag{6}$$

where $|g\rangle$ represents the global ground state where all molecules stay in their ground state and $a_i^{\dagger}$ creates a local excitation at the ith molecular site. For one-dimensional (1D) translational invariant systems with nearest-neighbor interactions ($E_i = E_{\text{ex}}, J_{ij} = J\delta_{j,i\pm 1}$), the Hamiltonian can be diagonalized by the Fourier transformation,

$$|k\rangle = \frac{1}{\sqrt{N}}\sum_{j} e^{ikj}\,|j\rangle,\ k = 0, \pm\frac{2\pi}{N}, \pm\frac{4\pi}{N}, \ldots, \pi \tag{7}$$

the states $|k\rangle$ represent a complete set of single-excitation states of the whole system. All $|k\rangle$ are coherently delocalized, with the phase coherence spreading over the whole aggregate. The Hamiltonian is diagonal in the k-space (momentum space) with the energy dispersion $E_k = E_{\text{ex}} + 2J\cos k$. The phase factor e^{ikj} determines the relative phase between monomers, and lead to different interference patterns. Considering the two limiting cases:

- For $|k = 0\rangle$, the phase factor is constant for all monomers, and all amplitudes add up constructively, leading to the bright state with the largest oscillator strength $|\langle\hat{\mu}\rangle|^2 = N\mu^2$ and energy $E_{\text{ex}} + 2J$. The dipole operator $\hat{\mu} = \mu\sum_i |i\rangle\langle g| + |g\rangle\langle i|$. For J-aggregate ($J < 0$), this corresponds to the lowest energy state, and the aggregate exhibits strong luminescence called superradiance and red-shifted absorption and emission spectra [27–31].
- For $|k = \pi\rangle$, the phase factor alternates sign between monomers, causing destructive interference. This state corresponds to the optically forbidden dark state with zero oscillator strength, and energy $E_{\text{ex}} - 2J$. For H-aggregate, this corresponds to the lowest energy state, and the aggregate is non-emissive. In the presence of temperature effects, disorder effects, vibronic effects and CT effects, the symmetry can be broken and leads to emissive H-aggregates [5, 7, 32–34], which we will discuss in the following sections.

Intermediate k values lead to states with varied interferences and will play important roles at finite temperatures. We move on to the discussion of the exciton coherence at finite temperature in the following section.

2.2 | Exciton Coherence at Finite Temperature

At finite temperature, the excitons are populated among all states, and typically the population thermalizes rapidly compared to the radiative decay rates and the Boltzmann distribution are established and maintained, thereby dictating the luminescence properties of the aggregate [35, 36].

$$\hat{\rho} = \frac{e^{-\beta\hat{H}}}{\mathrm{Tr}\left[e^{-\beta\hat{H}}\right]} = \sum_k p_k\,|k\rangle\langle k| \tag{8}$$

where $p_k = e^{-\beta E_k} / \sum_k e^{-\beta E_k}$. The transition dipole moment square of the molecular aggregate is given by the weighted sum,

$$I = \sum_k p_k\, I_k,$$

$$f_{\text{os},k} = \omega_{kg}\, I_k \tag{9}$$

where I_k is the transition dipole moment square that is proportional to the oscillator strength $f_{\text{os},k}$ for $|g\rangle \to |k\rangle$, and ω_{kg} corresponds to the energy difference between $|k\rangle$ and the ground state. Without assuming translational invariance, $|k\rangle$ can be

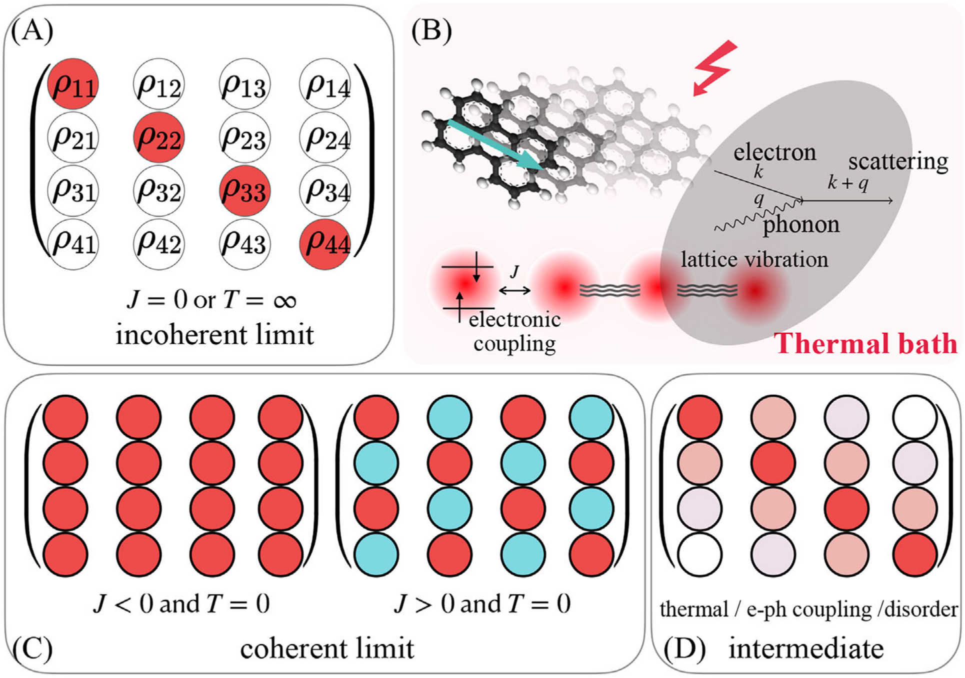

FIGURE 2 | Schematics of electron–phonon molecular aggregates at finite temperature and the electronic density matrix (site basis). The electronic density matrix at different regimes: (A) incoherent limit (zero intermolecular coupling or infinitely high temperature); (C) coherent limit (zero temperature) with coupling $|J| > 0$; (D) intermediate regime. (B) Model Hamiltonian with intermolecular couplings and electron–phonon couplings.

generally defined with a linear combination of local excited state (site basis), $|k\rangle = \sum_i c_{ki}|i\rangle$.

$$I_k = |\langle k\,|\hat{\mu}|\, g\rangle|^2 = \mu^2 \sum_{i,j} c_{ki}c_{kj} \tag{10}$$

and the total dipole square

$$I = \mu^2 \sum_{i,j}\left(\sum_k p_k c_{ki}c_{kj}\right) = \mu^2 \sum_{i,j}\rho_{ij} \tag{11}$$

This is known as the sum rule: the intensity reduces to the sum of all elements of the electronic density matrix in the site basis (up to a constant factor):

$$\rho = \begin{pmatrix} \rho_{11} & \rho_{12} & \cdots & \rho_{1N} \\ \rho_{21} & \rho_{22} & \cdots & \rho_{2N} \\ \vdots & \vdots & \ddots & \vdots \\ \rho_{N1} & \rho_{N2} & \cdots & \rho_{NN} \end{pmatrix} \tag{12}$$

Again, as graphically shown in Figure 2A,C, in the following limiting cases,

- *Coherent limit.* At $T = 0$, the thermal population is concentrated in the lowest state of the excited state manifold, and $\rho = |\mathrm{G}\rangle\langle\mathrm{G}|$. According to Equation (7),

$$\rho_{ij} = \begin{cases} \frac{1}{N} & \text{for J} - \text{aggregate}, |\mathrm{G}\rangle = |\, k = 0\rangle \\ \frac{(-1)^{i-j}}{N} & \text{for H} - \text{aggregate}, |\mathrm{G}\rangle = |\, k = \pi\rangle \end{cases} \tag{13}$$

which corresponds to complete coherence spreading all molecular sites. According to Equation (11), this leads to N times larger oscillator strength for J-aggregate and zero oscillator strength for H-aggregate (even number of monomers), which is consistent with our discussion in the previous section.

- *Incoherent (localization) limit.* At $T \to \infty$, the thermal population is uniformly distributed among all the states (i.e., $p_k = 1/N$), which leads to $\rho_{ij} = \delta_{ij}/N$, corresponding to the incoherent limit (no coherence between different states). According to Equation (11), this leads to the oscillator strength of μ^2 for both J-aggregate and H-aggregate, which is identical to the monomer.

Having examined the purely electronic effects, we now turn to vibronic coupling, the interaction between electronic and vibrational degrees of freedom that plays a crucial role in organic molecular aggregates.

2.3 | Soft Nature of Vibronic Frenkel Excitons

The ideal exciton is fully coherent over the entire domain for aggregates composed of N *disorder-free rigid* molecules at zero temperature. The inclusion of thermal dephasing effects leads to the reduction of coherence. In reality, even at low temperatures, the coherence of exciton is also limited by the exciton-vibrational (or exciton–phonon) couplings. Due to the soft nature [11, 12, 37–41], organic π-conjugated molecules undergo substantial structure reorganizations upon excitation and the exciton is spatially localized to a subset of the aggregate in sub-picoseconds or picoseconds due to the coupling to high-frequency modes [14, 42] or low-frequency modes [43, 44]. Continuing from the electronic Hamiltonian ($\hat{H}_\mathrm{e} = 2J \sum_k \cos k a_k^\dagger a_k$) that we introduced in Section 2.1, here we add an optical vibrational mode interacting with the electronic excitation, the Frenkel–Holstein Hamiltonian in momentum space can be written as

$$\begin{aligned} \hat{H} &= \hat{H}_\mathrm{e} + \hat{H}_\mathrm{ph} + \hat{H}_\mathrm{e-ph} \\ &= \hat{H}_\mathrm{e} + \omega \sum_q a_q^\dagger a_q + \tfrac{g\omega}{\sqrt{N}} \sum_{k,q} a_{k+q}^\dagger a_k \left(b_q^\dagger + b_q \right) \end{aligned} \tag{14}$$

where k and q correspond to the momentum of electrons and phonons. The second term represents the vibrational energy of phonon, and the last term describes electron–phonon interactions, corresponding to phonon absorption and emission processes, as illustrated in Figure 2B. In real space, the Hamiltonian can be expressed as

$$\hat{H} = \sum_{ij} J_{ij} a_i^\dagger a_j + \omega \sum_i b_i^\dagger b_i + g\omega \sum_i a_i^\dagger a_i \left(b_i^\dagger + b_i \right) \tag{15}$$

where i and j corresponds to the molecular site indices. This allows us to consider intermolecular couplings J_{ij} beyond nearest neighbors, without assuming translational invariance. In Equations (14) and (15), we use the second-quantized operators $a^\dagger(a)$ to denote electronic creation (annihilation), and $b^\dagger(b)$ for phonon mode creation (annihilation). The coupling strength g is called the electron–phonon coupling constant, and $S = g^2$ is the so-called Huang–Rhys factor. In realistic materials, usually, more than one vibrational mode are coupled to a single electronic degree of freedom [45–48].

As can be seen from Equations (14) and (15) and Figure 2B, the motion of the electron is coupled to the motion of the vibrational mode. Upon electronic excitation, the molecule undergoes structural reorganization, causing distortion of the surrounding lattice. This lattice distortion couples to and follows the electronic excitation, forming a quasi-particle called a polaron [12, 50–52]. The polaron represents the combined electronic excitation and its associated lattice deformation field. A useful quantity called vibrational distortional field (VDF) is defined to characterize the spatial extent of the vibrational dressing of polarons,

$$D(r) = \sum_i \left\langle a_i^\dagger a_i \frac{b_{i+r}^\dagger + b_{i+r}}{2} \right\rangle \tag{16}$$

which measures the spatial extent of the lattice distortion induced by a central electronically excited molecule. Specifically, it measures the average vibrational displacement from its S_0 minimum position for phonons that is r sites away from the electronic excited site. To get more familiar with the VDF, we consider the following limiting cases:

- $D(r) = -g\delta_{r,0}$ indicates that the exciton is fully localized (or trapped) and does not cause any lattice distortion around it.
- $D(r) = -g/N$ indicates that the exciton is fully delocalized and causes a uniform lattice distortion around it.

In Figure 3, we show the spatial distribution of the VDF for a 1D (Figure 3B) and a two-dimensional (2D) (Figure 3C) molecular aggregate in the intermediate regime. As the electronic coupling J increases, the lattice distortion effect becomes wider in space.

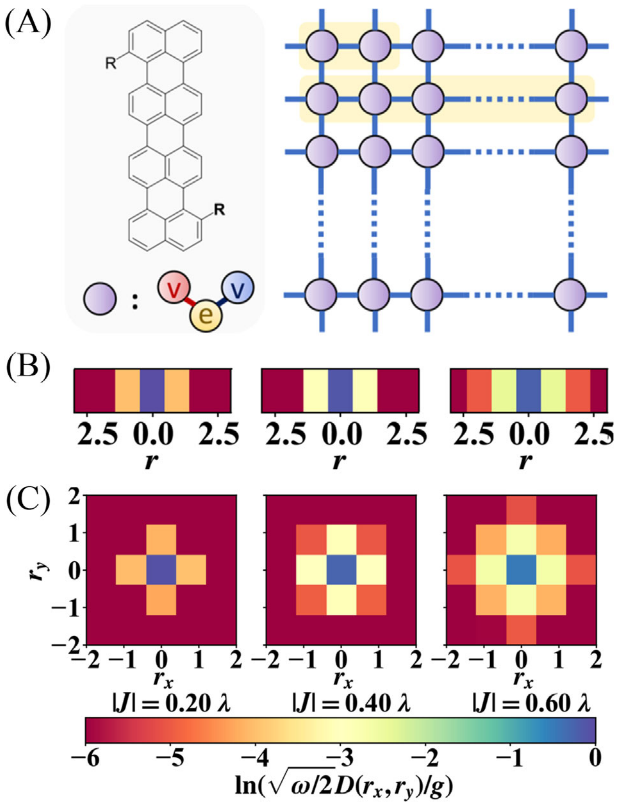

FIGURE 3 | Vibrational distortional field for a one-dimensional (B) and a two-dimensional (C) molecular aggregate. (A) Molecule that couples to two harmonic vibrational modes. Figure adapted from Ref. 49.

We now turn to the ECL, a metric that quantitatively measures the spatial coherence extent within the molecular aggregate.

2.4 | Exciton Coherence Length

ECL has been defined to measure the spatial distance over which the exciton is coherently delocalized [31, 54, 55]. As we discussed in previous sections, especially in the discussion on coherent and incoherent limits, the optical response is largely determined by exciton coherence. We refer interested readers to the review paper that elaborates on coherence in chemistry [56]. Chemical systems such as biological systems and optoelectric functional devices have been incorporating molecular aggregate with long ECL and thus enhanced optical responses [27–31] to enhance function. The studies of exciton coherence largely concentrated on the excited energy transfer [57], exciton transport [38, 58, 59], and luminescence properties [54, 60–62] of molecular aggregates. For instance, when there is one dominant high-frequency vibrational mode, as shown in Figure 4, the reduced emission spectra and ECL of a 60-sites linear J-aggregate aligns well with the ratio of the 0–0 and 0–1 peak [53]. Although unlike the direct comparison between the ratio and ECL for J-aggregate, the emission peak's ratio can be used to partially indicate the ECL and probe the amplitudes of static disorder in H-aggregate [32].

In Equation (12), we introduced that the off-diagonal terms of the electronic density matrix ρ_{ij} stores the quantum superposition information, which is, the *coherence* between molecular sites

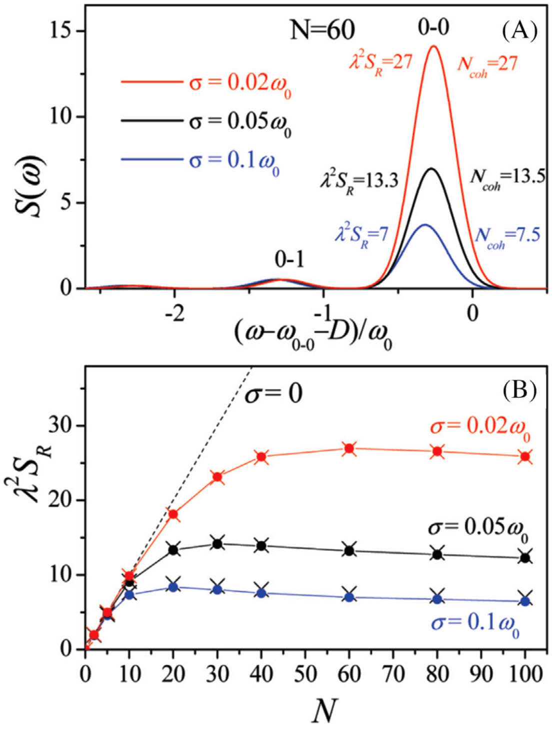

FIGURE 4 | Reduced emission spectra and exciton coherence length of a 60-site linear J-aggregate with different Gaussian static disorders, where the ratio of the 0–0 and 0–1 peak aligns well with the exciton coherence length. Figure adapted from Ref. 53.

i and j. The exciton reduced density matrix of the vibronic Frenkel exciton model, obtained by tracing the phonon degrees of freedom of the total density matrix [63–65], is the most relevant physical quantity to exciton coherence. The reduced density matrix depicts the system and serves as the initial state for quantum dynamics simulations of open quantum systems [66]. Note that there are also experimental protocols to measure the reduced density matrix by quantum tomography via ultrafast spectroscopy [64]. A frequently used quantity to characterize the exciton delocalization is the so-called participation ratio (PR) [67–75].

$$\mathrm{PR} = \mathrm{IPR}^{-1} = \frac{1}{\sum_i |\rho_{ii}|^2} \tag{17}$$

Inverse participation ratio (IPR) is the reciprocal of PR which ranges from 1 for fully localized state to N for fully delocalized state [67]. PR is useful when the translational invariance is broken, for example, in the presence of static disorders or open boundary conditions. For the translationally invariant system, as we mentioned in the previous section, it is a constant number. Moreover, PR does not consider the contribution of the off-diagonal terms. To address this concern, a straightforward definition of the exciton coherence function was proposed by Kühn and Sundström [76],

$$C(r) = \sum_i |\rho_{i,i+r}| \tag{18}$$

by summing over all off-diagonal terms that have the same spatial distance r, which measures the coherence at a certain distance r. A narrower $C(r)$ as a function of r indicates a more localized exciton, and a broader coherence function indicates a more delocalized exciton. It can also be expanded to cases where the static disorder is present, by averaging over different configurations [76]. In Equation (18), ρ can be a description for the total system which is generally a mixed state in the presence of thermal population, or can be a specific state of interest $|\psi\rangle$, such as the ground state or one of the excited states, by letting $\rho_{ij} = \langle\psi|a_i^\dagger a_j|\psi\rangle$, where one may also remove the absolute value in Equation (18) to observe the phase information of the coherence [32, 53, 77]. The ECL can be defined as [66, 76],

$$L_{\mathrm{coh}} = \sum_r C(r) \tag{19}$$

Exciton coherence functions related to the vibronic creation and annihilation operators $\tilde{a}_i^\dagger(\tilde{a}_i)$ were also defined where the phonons are in the vacuum state, which has shown in convenience in several studies [14, 32, 53, 77].

Mukamel and co-workers [54] proposed to measure the variance of the reduced density matrix as the coherence length,

$$L_{\mathrm{coh}} = \frac{\left(\sum_{mn} |\rho_{mn}|\right)^2}{N \sum_{mn} |\rho_{mn}|^2} \tag{20}$$

which gained great popularity in the field [66, 78–81]. However, as pointed out by Smyth et al. [55], the purity [purity(ρ) = Tr(ρ^2)] appears in the denominator by rewriting this expression, which makes L_{coh} decays too slow under decoherence because purity converges to $1/N$. The value of the purity changes from $1/N$ (fully mixed state) to 1 (pure state), which was also used to quantify the exciton entanglement [75]. In the single-exciton space, we discussed throughout this paper, the entanglement and coherence are necessary and sufficient conditions for the presence of each other [55, 82]. Inspired from the quantum information theory, Smyth et al. proposed the so-called tangles:

$$E_{\mathrm{T}}(\rho) = 4 \sum_{i,j>i}^{N} \left|\rho_{ij}\right|^2 = 2\left\{\mathrm{Tr}\left(\rho^2\right) - \mathrm{IPR}(\rho)\right\} \tag{21}$$

which combines the purity measure and IPR. It can also link to other multipartite entanglement measures [82–85]. They compared the tangles (Equation 21) with the variance (Equation 20) and the IPR (Equation 17) in observing the time-dependent dynamics of exciton coherence in the light-harvesting complex, and concluded that IPR totally fails for mixed state and the variance decays too slowly under decoherence.

The readers might notice that there is not a unique definition of the coherence length, and the choice of the definition depends on the specific system and the physical quantity of interest. The generalization of different definitions of ECL to complex cases is also questioned as different definitions of ECL lead to even qualitative differences for the temperature dependence of coherence [66]. Despite its drawbacks, the variance-based coherence length remains valuable for understanding energy transfer dynamics in complex systems [80, 81]. As we mention in Sections 2.1 and 2.2, for 1D periodic systems, increasing the excitonic coupling leads to larger ECL, resulting in stronger enhancement/suppression of the radiative rate for molecular aggregate with negative/positive couplings. This coupling patterns can be tuned by changing the packing angles, distances between molecules or the number of interacting molecules [31, 86–88]. A key question is how these various ECL measures correlate with the radiative efficiency of molecular aggregates. The radiative efficiency of molecular aggregate, when neglecting non-radiative decay pathways, can be defined as the following ratio between an N-site aggregate and an isolated molecule,

$$\gamma = \frac{\int d\omega I_N^\alpha(\omega)}{\int d\omega I_1^\alpha(\omega)} \tag{22}$$

$$I_N^\alpha(\omega) = \sum_{uv} \frac{e^{-\beta E_v}}{Z} \left|\langle \phi_u | \hat{\mu}_\alpha | \phi_v \rangle\right|^2 \delta(\omega - E_{uv}) \tag{23}$$

where $I_N{}^\alpha(\omega)$ is the expression of the dimensionless steady-state α-polarized fluorescence spectrum for N-site molecular aggregates. Accurate computation of emission spectra and the reduced density matrix for the vibronic Frenkel exciton model is challenging to most of the existing methods, due to the large number of vibrational modes and the associated large Hilbert space. We have developed numerically exact DMRG approaches [46, 47, 65, 89, 90] for such systems. We also proposed a new measure that directly correlates with radiative efficiency γ in molecular aggregates [62],

$$L_\rho = \left(\sum_{mn}^{N} \rho_{mn} + \frac{1}{N}\right)^{\Theta\left(\sum_{mn}^{N} \rho_{mn} - 1\right)} \tag{24}$$

where $\Theta(x)$ is a step function that is –1 for $x \leq 0$ and 1 for $x > 0$. This function builds a monotonic and bijective correlation between ECL and radiative efficiency for superradiant or subradiant aggregates. It is useful to analyze the limiting cases. In the complete coherence limit of superradiant ($\gamma > 1$) and subradiant ($\gamma < 1$) molecular aggregates, the reduced density matrix is ideally formulated as:

$$\rho_{mn} = \frac{1}{N},\ L_\rho = N + \frac{1}{N} \sim N \quad \text{superradiant} \tag{25}$$

$$\rho_{mn} = \frac{(-1)^{m-n}}{N},\ L_\rho = N \quad \text{subradiant} \tag{26}$$

In the complete localization limit for both superradiant and subradiant aggregates

$$\rho_{mn} = \frac{\delta_{mn}}{N},\ L_\rho = \frac{N}{(N+1)} \sim 1 \tag{27}$$

Starting from the reduced density matrix, a determined value of ECL is connected with the γ, which is different from previous definitions that have non-bijective connections. The new definition of ECL bridges the bijective relationship with the superradiance enhancement (SRE) of 2D aggregate, as shown in Figure 5B,D, which is defined as the *enhanced* ratio of the oscillator strength of molecular aggregate over that of an isolated molecule ($\gamma > 1$ in Equation 22). As shown in Figure 5, other previously defined ECLs show non-monotonic relation with the radiative efficiency. We can efficiently obtain the SRE of large-scale 2D aggregate (10 × 10). This allows us to look into the function–structure relationship of 2D aggregates including but not limited to the brick-layer setup we used here [91]. We study the temperature dependence of the SRE. It is also related to the concept of quantum Fisher information that measures the multipartite entanglement in quantum metrology of exciton system [92]. Previous studies have shown that SRE in 2D systems decrease with increasing temperature, following a $1/T$ law and reaching maximal SRE at zero temperature [61, 93]. Contrastingly, we observed novel temperature dependences of SRE in slipped 2D molecular aggregates, where SRE exhibits non-monotonic behavior and attains a maximum at a finite temperature $T(\gamma_{\max}) > 0$, as depicted in Figure 5C. Four exemplary cases with different packings are provided to show the different temperature dependencies of SRE and the ECL. For case A, the SRE increases with temperature, defying the behavior of traditional J-aggregates where SRE decreases due to reduced population in the lowest excited state at higher temperatures. It is also unlike H-aggregates, where radiative efficiency increases but does not exceed 1. Case A shows superradiance with efficiency growing beyond 1 as the temperature rises. It can seen that the lower energy states are generally coherent dark states, therefore at low temperatures, case A shows a very high ECL but small oscillator strength. As temperature increases, the population of the high bright states keeps increasing, leading to the increase of SRE and the decrease of ECL. In contrast, case D aligns with traditional J-aggregate behavior, exhibiting decreasing SRE with increasing temperature. Cases B and C display a peak in SRE at intermediate temperatures, initially increasing due to thermal activation and then decreasing at higher temperatures. This behavior is explained by the distribution of oscillator strength across energy levels obtained from diagonalizing the exciton Hamiltonian.

The new unified definition of ECL in Equation (24) building on the oscillator strength sum rule (Equation 11), provides a consistent, bijective relationship between ECL and radiative efficiency across both superradiant and subradiant 1D [62] and 2D aggregates. This ECL metric offers a reliable measure of coherence for assessing optical properties such as superradiance in complex systems.

3 | Role Of Intermolecular Charge Transfer for Excited State Structure in Aggregate

Besides the vibronic coupling effect, which is not included in conventional Kasha theory, the ICT effect serves as another complement to Kasha theory. When molecules are densely packed, the increase in wavefunction overlaps, resulting in larger transfer integrals. Meanwhile, as the distance between molecules decreases, the energy of the ICT state is reduced [94, 95]. The combination of large transfer integrals and lower ICT energy can cause the ICT state to participate in the lowest excited state, thus influencing the luminescence behavior of the aggregates [5, 6].

3.1 | CT-Mediated Aggregates

The relationship between the ICT state/CT exciton and the localized Frenkel exciton is illustrated in Figure 6. When the energy of the CT exciton (E_{CT}) is close to the monomer exciton energy (E), the contribution of CT exciton needs to be included in the total Hamiltonian [6, 96–98]. However, when $|E_{\mathrm{CT}} - E| \gg |t_{\mathrm{e}}|, |t_{\mathrm{h}}|, |J|, |\omega_{\mathrm{vib}}|$, where t_{e}, t_{h}, and J represent electron transfer integral, hole transfer integral, and exciton coupling, respectively,

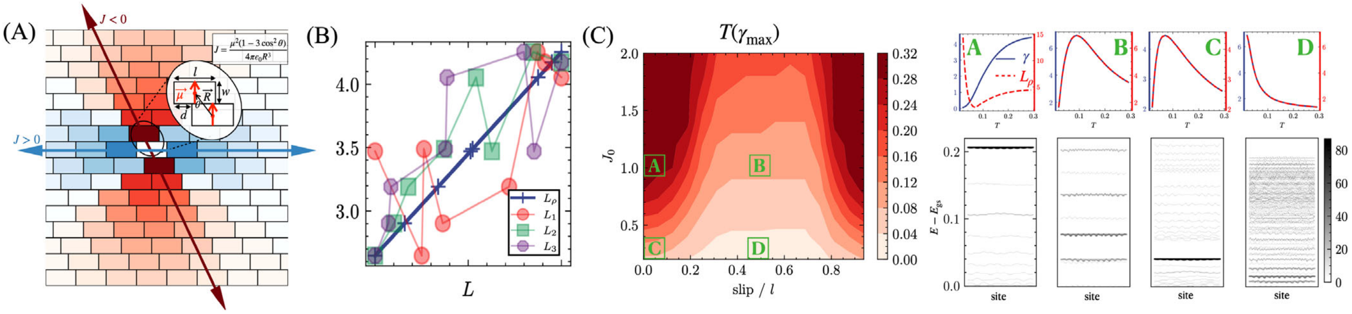

FIGURE 5 | (A) Brickwork packing of two-dimensional molecular aggregates. (B) Correlation between the radiative efficiency and the exciton coherence length with different definitions of exciton coherence length (ECL). L_1 refers to the ECL defined in Equation (20), and L_2 refers to the ECL defined in Equation (19), and L_3 refers to the ECL defined by purity. (C) The temperature of realizing maximum superradiance for different slip distances and couplings. Four exemplary cases that illustrate the temperature dependence of γ and L_ρ. The corresponding wavefunctions with combining coefficients for the local site, whose color depth indicates the oscillator strength of that energy level. Figure adapted from Ref. 62.

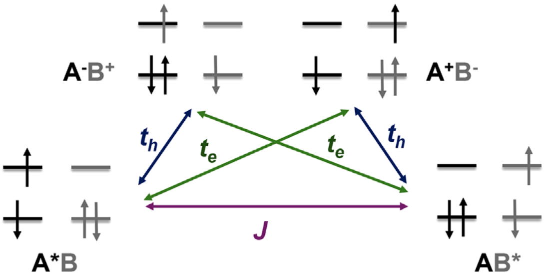

FIGURE 6 | Schematic graph of the couplings between Frenkel excitons (A*B and AB*) and charge transfer (CT) excitons (A^-B^+ and A^+B^-).

as shown in Figure 6; ω_{vib} is the vibration energy, a second-order perturbative approach can be employed to directly obtain the exciton coupling induced by the CT exciton (J_{CT}) [96, 97]:

$$J_{CT} = -2\frac{t_e t_h}{E_{CT}-E} \tag{28}$$

From Equation (28), the sign of J_{CT} depends on the relative signs of t_e and t_h as well as the energy ordering between E_{CT} and E. Specifically, when $J_{CT} < 0$, the CT exciton induces J-aggregate behavior; conversely, when $J_{CT} > 0$, it leads to H-aggregate behavior. By combining this with conventional long-range Coulomb exciton coupling (J), a variety of new aggregate types can be formed, designated as HH, HJ, JH, and JJ aggregates. In these designations, the first letter represents the effect of exciton coupling, while the second letter corresponds to the effect of the CT exciton [5, 6].

Moreover, based on Fermi's golden rule for systems in the hopping regime, charge mobility is proportional to the square of the transfer integral; and for other transport regimes such as band-like transport, there is also a positive correlation between mobility and transfer integral magnitude. This relationship arises because larger transfer integrals enable better charge delocalization and transport, leading to enhanced carrier mobility. Strategic incorporation of ICT can potentially balance luminescence and charge transport, two properties that were generally considered mutually exclusive [7, 99].

3.2 | Three-State Model for Dimer—A Primer for Herringbone Stacking

Due to the fact that the currently reported high-mobility emissive molecules are predominantly arranged in a herringbone packing structure [100], we initially investigated the mechanisms that allow charge transport and luminescence within this specific packing arrangement [7]. In a 2D herringbone lattice, one molecule can form four T-shaped dimers (face part: F; edge part: E) and two slipped π–π stacking dimers with its nearest neighbors (Figure 7A). Although the properties of the two slipped π–π stacking dimers are generally equivalent, the four T-shaped stacking dimers may exhibit slight variations due to small differences in centroid distances. We focus on the T-shaped stacking dimer with the shortest centroid distance and compare its properties with those of the slipped π–π stacking dimer. The investigated herringbone packing molecules are shown in Figure 7B. As illustrated in Figure 7D, the intermolecular dispersion predicted by the extended symmetry-adapted perturbation theory (XSAPT) and the many-body dispersion method (MBD) (XSAPT + MBD) [101] is consistently stronger in T-shaped dimers than in slipped π–π stacking dimers across all the aggregates examined. Furthermore, according to the point-dipole approximation, exciton coupling J is inversely proportional to the cube of the centroid distance between two monomers. Consequently, the T-shaped stacking dimer also exhibits stronger J compared to the slipped π–π stacking dimers due to its shorter centroid distance. Consequently, a T-shaped dimer, anticipated to exhibit a more pronounced aggregation effect than the slipped π–π dimer due to its stronger intermolecular interactions and exciton coupling, is selected to investigate the luminescence properties of the aggregates.

In T-shaped dimers, two types of CT excitons are formed, designated as F^+E^- (charge transferred from the face part to the edge part) and F^-E^+ (charge transferred from the edge part to the face part). The excitation energies of F^-E^+ and F^+E^- for all investigated systems are presented in Figure 7C, alongside the S_1 excitation energies of the monomers for comparison. It is evident that F^-E^+ has a significantly lower energy than F^+E^- and is closely aligned with the locally excited S_1 state. This energy difference can be attributed to varying intermolecular interactions within these two CT excitons. As shown in Figure 7E, the overall attraction within F^-E^+ is stronger than that within F^+E^-, primarily due

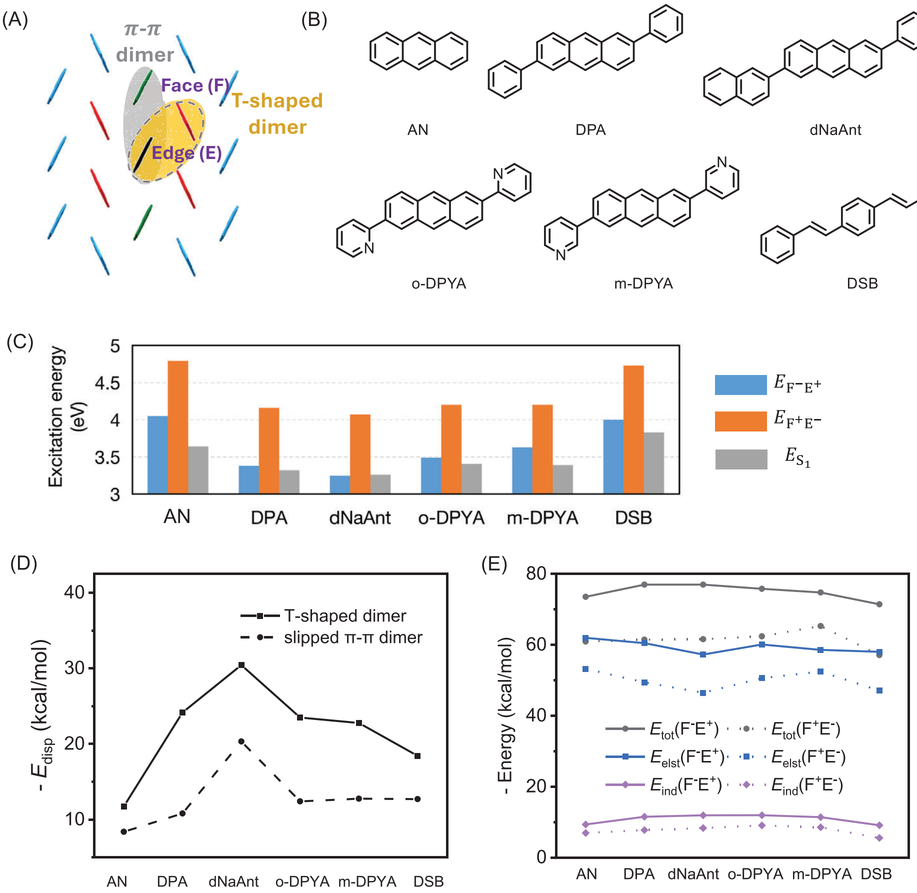

FIGURE 7 | Herringbone packing pattern, systems, energy, and interactions. (A) Two-dimensional herringbone lattice; (B) investigated herringbone molecules; (C) local excited S_1 energy of the monomer and intermolecular charge transfer (ICT) energies; (D) dispersion energy in two kinds of dimer in herringbone packing; (E) calculated intermolecular interactions in two ICT (F^-E^+ and F^+E^-) states. Figure adapted from Ref. 7.

to larger electrostatic and induction interactions. This stronger attraction stabilizes the energy of F^-E^+, making it energetically feasible for F^-E^+ (rather than F^+E^-) to couple with the locally excited states of the monomer. The energies of the two types of CT states are calculated in the vacuum phase in this study. It is important to note that when the dimer is embedded in a crystal, the polarizable effect would lead to a reduced energy separation [102]. We employed the QM/MM method to account for the polarization effect [7]. The systems investigated in Figure 7B exhibit a significant CT energy difference (>0.35 eV) in the QM/MM calculations, under which the three-state model is applicable. However, when the energy difference becomes sufficiently small, the four-state model, as discussed below, should be utilized.

Since only one CT exciton (F^-E^+) is energetically favorable for coupling with the locally excited state of each monomer (denoted as F^*E and FE^*) in the T-shaped dimers of herringbone aggregates investigated in this work, three-state model could be established in the basis of $\{|F^*E\rangle; |FE^*\rangle; |F^-E^+\rangle\}$:

$$\hat{H} = \begin{bmatrix} E & J & t_h \\ J & E & t_e \\ t_h & t_e & E_{CT} \end{bmatrix} \tag{29}$$

E is the S_1 excited state energy of the monomer, t_e is electron transfer integral, and t_h is hole transfer integral. After applying the block diagonalization, we could obtain a three-state model on the basis of Frenkel exciton and CT exciton $\{|FE_{AS}\rangle, |FE_S\rangle, |F^-E^+\rangle\}$:

$$\hat{H} = \begin{bmatrix} E - J & 0 & \frac{\sqrt{2}}{2}(t_h - t_e) \\ 0 & E + J & \frac{\sqrt{2}}{2}(t_h + t_e) \\ \frac{\sqrt{2}}{2}(t_h - t_e) & \frac{\sqrt{2}}{2}(t_h + t_e) & E_{CT} \end{bmatrix} \tag{30}$$

where $|FE_S\rangle = \frac{\sqrt{2}}{2}(|F^*E\rangle + |FE^*\rangle)$, $|FE_{AS}\rangle = \frac{\sqrt{2}}{2}(|FE^*\rangle - |F^*E\rangle)$. $|FE_S\rangle$ is a bright state because the transition dipole moments add constructively, resulting in a dipole moment that is two times that of the monomer. In contrast, $|FE_{AS}\rangle$ is a completely transition dipole-forbidden dark state because the transition dipole moments cancel each other out.

In H-aggregates, where $J > 0$, the $|FE_{AS}\rangle$ state is lower in energy, leading to quenching of luminescence within the aggregates. However, if the CT exciton is incorporated with the Frenkel exciton and the coupling between the CT exciton $|F^-E^+\rangle$ and $|FE_S\rangle$ is sufficiently strong, the H-aggregate can become emissive and may even exhibit J-aggregate behavior (Figure 8A). When $E_{CT} = E + J$, by diagonalizing Equation (30) and assuming that the absolute values of t_e and t_h are equal, we obtain the condition $t_h \approx t_e > \sqrt{2}|J|$ for achieving an emissive H-aggregate. This implies that relatively large (compared to J) and same signed t_e

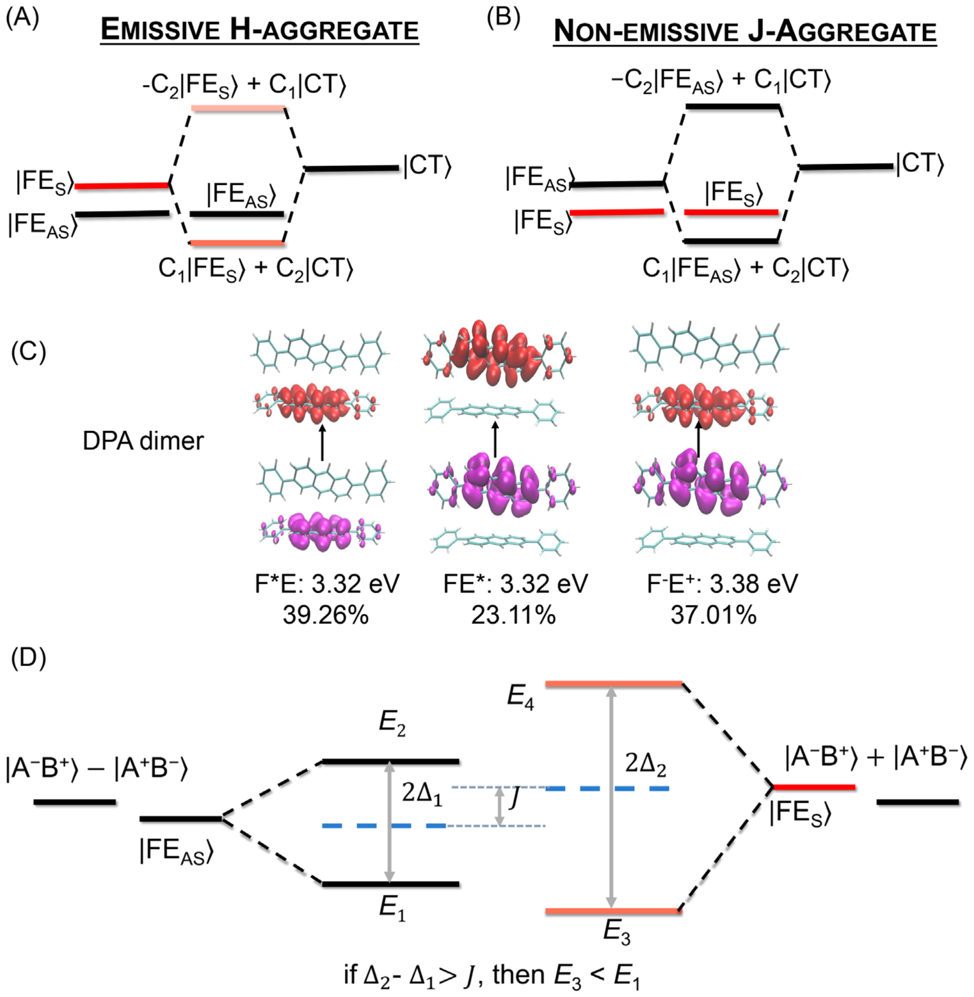

FIGURE 8 | Three-state model for emissive H-aggregate (A) and non-emissive J-aggregate mechanism (B). The intensity of the red color indicates the strength of the transition dipole moment: a more saturated red signifies a stronger transition dipole moment, while black represents transition-dipole-forbidden dark states. (C) Attachment–detachment densities and excitation energies for the diabatic states in the DPA [103] T-shaped dimer. The percentages listed below each excitation energy represent the proportion of the corresponding diabatic state's contribution to the adiabatic S_1 state in DPA. (D) Schematic graph of the four-state model in—packing aggregates. Figure adapted from Refs. 7 and 99.

and t_h are favorable for luminescence. Under such conditions, large transfer integrals are beneficial to high mobility, thereby making the coexistence of high luminescence and efficient charge transport achievable. Conversely, relatively large (compared to J) but oppositely signed t_e and t_h could result in the quenching of emissive J-aggregates (Figure 8B).

Using the three-state model, we have successfully explained the phenomenon of enhanced radiative rates and red-shifted absorption spectra observed upon aggregation in high-mobility emissive materials [7, 103, 104]. The contributions of the three states can be determined not only through direct diagonalization of Equation (29), but also using diabatization methods such as Boys diabatization [105], as illustrated in Figure 8C.

3.3 | Four-State Model for Dimer—A Primer for π–π Stacking

π–π stacking is widely recognized as the most effective arrangement for achieving high carrier mobility [13]. Understanding the conditions that enable both high mobility and strong light emission in such systems is highly desirable [99]. In π–π stacking, a dimer typically features two degenerate CT excitons, A^-B^+ and A^+B^-, whereas this energy degeneracy is generally not maintained in herringbone structures. Therefore, a four-state model Hamiltonian, encompassing the local Frenkel excitons A^*B and AB^*, as well as the ICT excitons A^-B^+ and A^+B^-, is necessary to accurately describe π–π stacking:

$$\hat{H} = \begin{bmatrix} E & J & t_h & t_e \\ J & E & t_e & t_h \\ t_h & t_e & E_{CT} & 0 \\ t_e & t_h & 0 & E_{CT} \end{bmatrix} \tag{31}$$

The coupling between the two CT excitons, A^-B^+ and A^+B^-, consists of intermolecular and intramolecular exchange integrals, which are small enough to be neglected. Therefore, in Equation (31), the coupling is set to zero. Similarly, after block-diagonalizing Equation (31), as shown in Figure 8D that the bright state $|FE_S\rangle$ only couples with the symmetric CT exciton $|A^-B^+\rangle$ +

$|A^+B^-\rangle$, while the dark state $|FE_{AS}\rangle$ exclusively couples with the anti-symmetric CT exciton $|A^-B^+\rangle - |A^+B^-\rangle$. To achieve both high mobility and high luminescence in the aggregate simultaneously, the condition $E_3 < E_1$ must be satisfied. This requires t_e and t_h to have the same sign and be sufficiently larger than J, similar to the requirements in herringbone packing.

3.4 | Molecular Descriptor for Realizing High Mobility and High PLQY

Diagonalizing the parameter matrix in Equation (29) or (30) results in tedious and complex expressions, which are not conducive to analysis [7]. However, by directly diagonalizing Equation (31), it is straightforward to obtain the condition for high mobility and emissivity ($E_3 < E_1$ in Figure 8D), which yields $J \le \frac{2t_e t_h}{|t_e + t_h|}$. Based on this equation, we established a descriptor I to characterize mobility and PLQY:

$$I = \frac{2t_e t_h}{(|t_e| + |t_h|)\,|J|} \tag{32}$$

The reason we choose $|t_e| + |t_h|$ instead of $|t_e + t_h|$ is that when t_e and t_h have opposite signs, I would be particularly negative if we used $|t_e + t_h|$. We use $|J|$ here because, in J-aggregates ($J < 0$), t_e and t_h also need to have the same sign, similar to H-aggregates. According to the results of the four-state model, I should be equal to or greater than 1.0 for optical emission to be allowed in π–π stacking cases. This condition is more general since we do not impose the constraint of equal amplitudes for t_e and t_h, which was imposed in our previous work for convenience in herringbone materials. We believe that this descriptor can also be applied to herringbone materials, which can be considered a specific case of the four-state model. To identify the conditions for high mobility and emission in herringbone materials, we conducted a model case study, finding that the criterion is $I > \sqrt{2}$. Therefore, we use $I > 1$ as the criterion for π–π stacked crystals and $I > \sqrt{2}$ for herringbone crystals to screen for high-performance, high-mobility emissive materials.

3.5 | Molecular Packing Effect for Realizing High Mobility and High PLQY

Based on the above discussion, the key factors are the values of t_e, t_h, and J [7, 99]. These factors are highly sensitive to the frontier orbital node pattern and packing geometries. In eclipsed packing, the molecules are aligned in the same orientation (Figure 9A), while in staggered packing (Figure 9B), the molecules are aligned in opposite orientations. We have shown that eclipsed packing in herringbone stacking molecules is favorable, as t_e and t_h typically have the same sign along the different long and short axes (Figure 9C), which is beneficial for luminescence. This is observed in molecules such as DPA, dNaAnt, and AN, which exhibit enhanced radiative rates upon aggregation. In contrast, in staggered stacking within herringbone materials, t_e and t_h generally have opposite signs (Figure 9D), which is detrimental to luminescence, leading to reduced radiative rates upon aggregation, as seen in o-DPYA and m-DPYA materials [106].

The descriptor I we proposed can be directly applied to screen for favorable packing geometries and potential candidates.

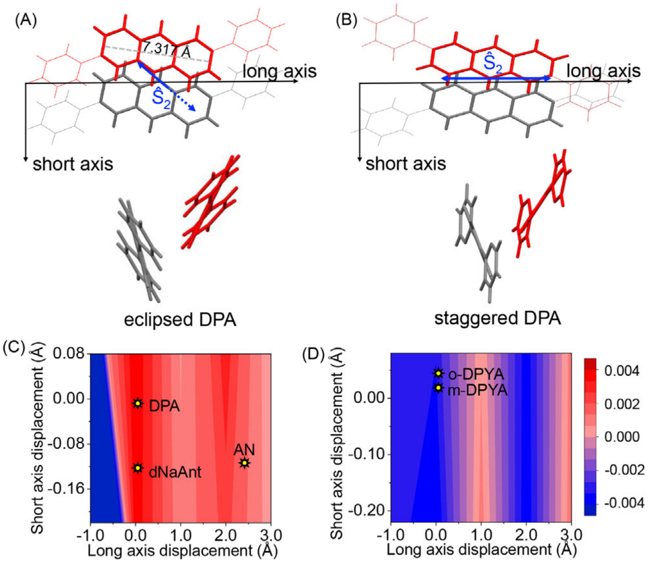

FIGURE 9 | Two packing motifs in T-shaped DPA dimers: (A) eclipsed and (B) staggered; the effect of the packing motif on the transfer integral sign, $t_h \times t_e$, concerning displacements along the short and long axes in (C) eclipsed dimers and (D) staggered dimers. Figure adapted from Ref. 7.

Anthracenes, carbazoles, and fluorenes are commonly used as key units in either highly emissive or high-mobility organic electronic materials. Through quantum chemical calculations, we demonstrate the values of J, t_e, t_h, and I as a function of lateral displacement in these three types of materials. The criteria are $I > 1$ for π–π stacked crystals and $I > \sqrt{2}$ for herringbone crystals. Our conclusion is that molecules with acene-like frontier molecular orbitals (MOs) combined with an eclipsed packing mode, or molecules with carbazole-like frontier MOs in π–π stacking, are more likely to achieve both high mobility and high luminescence.

Fused ring compounds are often used as building blocks or core units in high-mobility materials or luminescence materials. For example, anthracene (**1**) exhibits a PLQY of 0.24 in solution, which is enhanced to 0.64 in crystal [107], and achieves a mobility of 3 cm^2 V^{-1} s^{-1} in single-crystal OFET devices. Carbazole (**4**) and BTBT (**14**) are well-known for their high luminescence or high mobility. Compounds such as NDT [108] (**13**), ABT [109] (**19**), ADT [110] (**24**), DNTT [111] (**29**), and BTAT [112] (**30**) are recognized for their excellent transport properties and high mobility. We examine 32 fused ring compounds (Figure 10A), including three-ring fused molecules (**1**–**8**), four-ring fused molecules (**9**–**16**), five-ring molecules (**17**–**28**), and six-ring molecules (**29**–**32**).

The 32 fused-ring compounds were categorized into three groups based on their MO nodal distribution patterns. Group I includes compounds **1**, **2**, **9**, **10**, **11**, **12**, **13**, **14**, **15**, **17**, **19**, **21**, **23**, **24**, **26**, **29**, and **30**, all of which feature an acene-like frontier orbital nodal structure. Group II consists of compounds **4**, **6**, **8**, **18**, **22**, and **28**, which possess carbazole like frontier orbitals. Group III comprises compounds **3**, **5**, **7**, **16**, **20**, **25**, **27**, **31**, and **32**, all of which exhibit fluorene-like MOs. The calculated I values for these 32 fused rings are presented in Figures 10B. All eclipsed packing molecules in group I satisfy the high-mobility emissive

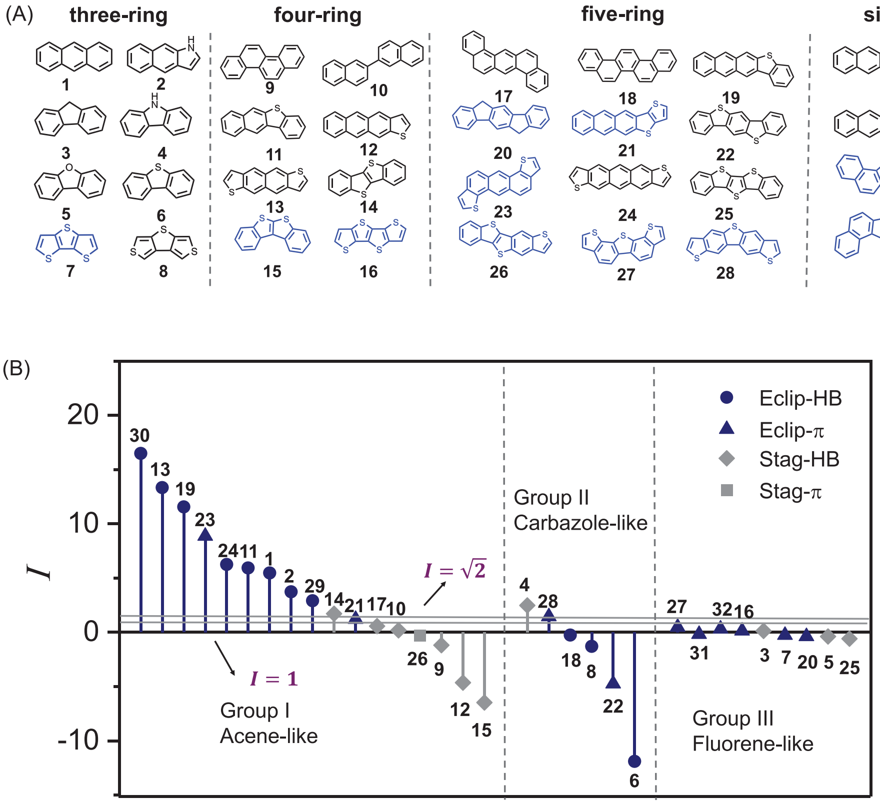

FIGURE 10 | (A) Molecular structures of the investigated fused rings, with π–π stackings highlighted in blue and the remaining structures exhibiting herringbone packing. (B) Calculated I values for the 32 fused rings. Figure adapted from Ref. 99.

condition defined by the I descriptor ($I > \sqrt{2}$ in herringbone crystals and $I > 1$ in π–π stacking crystals). However, only one staggered herringbone compound, **14** (BTBT), has an I value greater than $\sqrt{2}$, aligning with the discussion above. The other staggered stacking materials fail to meet the criteria due to either the opposite signs of t_e and t_h (**9**, **12**, **15**, and **26**) or significant imbalance between t_e and t_h (**10** and **17**).

Promising candidates include herringbone stacking molecules **1** (anthracene, I = 5.47), **2** (I = 3.73), **11** (I = 5.93), **13** (NDT, I = 13.34), **14** (BTBT, I = 1.72), **19** (ABT, I = 11.56), **24** (ADT, I = 6.26), **29** (DNTT, I = 2.91), and **30** (BTAT, I = 16.50) in group I, and eclipsed π–π stacking materials **21** (ATT, I = 1.20) and **23** (BADT, I = 8.87) in group I. In groups II and III, only staggered herringbone stacking **4** (carbazole, I = 2.48) and eclipsed π–π stacking **28** (I = 1.45) in group II meet the I criterion, which is consistent with our earlier discussion.

Thus, the I descriptor, derived from the model Hamiltonian, effectively demonstrates the relationship between packing modes and luminescence transport properties, while also providing a cost-effective method for screening high-mobility emissive candidates.

4 | Non-Radiative Decay Rate for Aggregates

In molecular aggregates, intermolecular excitonic coupling or CT states can alter the transition dipole moment, thereby either enhancing or suppressing radiative transitions [5, 6]. The previous two sections discussed the luminescent properties of aggregates from this perspective. In addition to radiative transitions, non-radiative transitions also play a crucial role in determining luminescent properties. Non-radiative decay involves dissipating the energy of the electronic excited state into molecular vibrations via electron-vibration coupling, which is subsequently transferred to the environment. The overall PLQY is given by $\eta = k_r/(k_r + k_{nr})$.

Molecular aggregates exhibit two main scenarios in their electronic excited states. In the first, the excited states remain localized, similar to those in individual molecules. In such a case, the non-radiative decay theory for single molecules can be extended by accounting for electrostatic polarization and steric effects from surrounding molecules. QM/MM multiscale simulations have proven effective in this context [113, 114]. In the second scenario, aggregation leads to significant changes in excited states, such as the formation of ICT states or delocalized exciton states. Here, the non-radiative decay of aggregates cannot be adequately described by single-molecule theory, necessitating new theoretical and computational approaches [49, 115–118]. In this section, we will discuss theoretical approaches and key findings regarding non-radiative decay rates for aggregates in these two scenarios.

4.1 | TVCF Theory for Molecular k_{nr}

In the first scenario, where the excited states of an aggregate remain localized on individual molecules, the non-radiative decay theory for single molecules can be applied. For luminescent molecules, non-radiative decay generally occurs on a nanosecond timescale, around three orders of magnitude slower than what state-of-the-art non-adiabatic dynamic methods can simulate [119, 120]. A feasible approach, therefore, is to use rate theory. Assuming (i) the initial state is in thermal equilibrium, meaning internal conversion among excited states and vibrational relaxation occur much faster than the transition to the ground state, and (ii) the non-adiabatic coupling between excited and ground states is small and thus can be treated perturbatively, the non-radiative decay rate can be expressed using Fermi's golden rule (in atomic units):

$$k_{\mathrm{nr}} = 2\pi \sum\nolimits_{uv} P_u \left| H_{1,fv,iu} \right|^2 \delta \left(E_{iu} + \Delta E_{\mathrm{ad}} - E_{fv} \right) \tag{33}$$

$$\hat{H}_1 = \sum_l F^l_{fi}\,(q) \left| \phi_f \rangle \langle \phi_i \right| \hat{p}_l + \mathrm{h.c.} \tag{34}$$

$$F^l_{fi}\,(q) = \left\langle \phi_f \left| \hat{p}_l \right| \phi_i \right\rangle \tag{35}$$

where $iu(fv)$ indicates the uth(vth) vibrational state of the initial(final) electronic state $\phi_i(\phi_f)$, $P_u = e^{-\beta Eiu}/Z(\beta)$ is the Boltzmann distribution of the initial state at temperature $\beta = 1/T$, and F^l_{fi} represents the non-adiabatic coupling constant for the lth vibrational mode.

Directly calculating the rate k_{nr} with Equation (33) involves summing over all vibrational states, which scales exponentially with the number of vibrational modes. To simplify, a Fourier transform is often applied to transition into the time domain:

$$k_{\mathrm{nr}} = \int_{-\infty}^{\infty} e^{i\Delta E_{\mathrm{ad}} t} C\,(t)\; dt \tag{36}$$

$$C\,(t) = \langle \hat{H}_1\,(t)\,\hat{H}_1 \rangle_T = \mathrm{Tr} \left(\frac{e^{-\beta \hat{H}_i}}{Z\,(\beta)} e^{i\hat{H}_i t} \hat{H}_1 e^{-i\hat{H}_f t} \hat{H}_1 \right) \tag{37}$$

Then, the focus shifts to the calculation of the time correlation function $C(t)$. Early foundational work by Huang and Rhys developed a non-radiative decay theory for color centers in polar solids, employing a displaced harmonic oscillator model and Fermi's golden rule to treat nuclear motion as a perturbation [121]. Lin further extended this theory to molecular internal conversion and intersystem crossing and showed that these rates can be obtained from ab initio quantum chemistry calculations [122, 123]. Englman and Jortner subsequently provided analytical expressions for decay rates in the strong or weak electron-vibration coupling regimes, with the latter known as the "energy gap law," predicting an exponential or super-exponential increase in decay rate with narrowing energy gaps [124]. The energy gap law has been widely confirmed by experiments.

However, previous methods for calculating $C(t)$ have two major limitations: (i) the promoting mode approximation [125], which assumes a single dominant mode for non-adiabatic coupling, is often inadequate for complex molecules, as multiple modes typically contribute; and (ii) mode mixing between ground and excited states (the Duschinsky rotation effect) complicate calculations. While Lin successfully addressed partial mode mixing and demonstrated its importance in affecting non-radiative decay, its full inclusion remains challenging [126]. To overcome the promoting-mode approximation and fully incorporate the Duschinsky rotation effect, our group has derived an elegant analytical expression for $C(t)$, which is called the thermal vibration correlation function (TVCF) theory [127–130]. This expression is exact under the harmonic approximation for the potential energy surface (PES) and scales computationally as $O(N^3)$ with the number of vibrational modes, making it suitable for very large molecular systems. TVCF has been successfully applied to calculate non-radiative decay rates for single molecule and has been used to predict fluorescence and phosphorescence spectra, radiative rates, intersystem crossing, and reverse intersystem crossing rates [130, 131]. Based on the TVCF theory, we have developed a software, called MOlecular MAterial Property Prediction Package (MOMAP) [132], which is widely used not only by theorists but also by experimentalists. Moreover, many research groups have adopted our method in their computational programs [133–135].

To account for aggregation effects, we have combined TVCF with multiscale computational methods that incorporate the electrostatic polarization and steric effects of neighboring molecules within aggregates. This approach has successfully clarified the mechanism of AIE [136]. By comparing non-radiative decay rates for single molecules and aggregates, we have demonstrated that steric hindrance within aggregates significantly reduces electron-vibration coupling of low-frequency vibrations, thereby lowering the non-radiative decay rate [113, 114].

4.2 | Extension of TVCF for Molecular Aggregates Through Time-Dependent DMRG

In systems involving energy or CT between aggregated molecules, we must go beyond the single-molecule theory. Eisfeld et al. modeled excited-state decay dynamics in molecular aggregates using the Redfield master equation, showing that excitonic coupling significantly impacts non-radiative decay rates [116]. Recently, we extended the single-molecule non-radiative decay rate theory to handle molecular aggregates with excitonic coupling effects [49]. The Hamiltonian for a molecular aggregate can be expressed as:

$$\hat{H}_0 = \sum_i \varepsilon_i \left| i \rangle \langle i \right| + \sum_{ij} J_{ij} \left| i \rangle \langle j \right| + \sum_{il} c_i \left| i \rangle \langle i \right| \hat{x}_{il} + \sum_{il} \frac{1}{2} \left(\hat{p}^2_{il} + \hat{x}^2_{il} \right) \tag{38}$$

where $|i\rangle$ represents the local excitation of the ith molecule, with other molecules in their ground states. The non-adiabatic couplings of all molecules in the aggregates are treated as perturbations together:

$$\hat{H}_1 = \sum_{i,l} \left(F^l_{gi} \left| g \rangle \langle i \right| + \mathrm{h.c.} \right) \hat{p}_{i,l} \tag{39}$$

$$F^l_{gi} = \left\langle g \left| \hat{p}_{i,l} \right| i \right\rangle \tag{40}$$

Unlike the single molecule case, the involvement of multiple coupled excited states introduces vibronic effects, which makes calculating the time correlation function $C(t)$ in Equation (37) very challenging. Full quantum dynamic simulation becomes exponentially complex with increasing vibrational modes, rendering it impractical for large systems. To address this, we developed a TD-DMRG algorithm, which approximates the high-dimensional wave function tensors as products of low-dimensional tensors, largely reducing computational complexity to a polynomial scale [46, 65]. Benchmark studies have demonstrated that TD-DMRG is highly accurate and efficient for simulating the time evolution of systems with complex electron-vibration coupling [65]. With TD-DMRG, we can compute $C(t)$ and, thus, the non-radiative decay rate with near-exact accuracy. This method has several key features: (i) in addition to the molecular parameters of a single molecule, it requires only the excitonic coupling constant J, which can be calculated via ab initio quantum chemistry. When $J = 0$, the theory reverts to the single-molecule case; (ii) being a numerical method, TD-DMRG is not limited to the harmonic approximation, allowing for the inclusion of anharmonic effects in the PES. Our recent work examined how such anharmonicity influences non-radiative decay rates, revealing that mode coupling can enhance the decay rate by several times [137, 138]. Finally, while Equation (38) considers only excitonic coupling (energy transfer) as discussed in Section 2, this method can be similarly applied to CT state, as introduced in Section 3.

4.3 | Non-Radiative Decay Rate for Aggregates: From Dimer to Linear Chain and Planar Cluster

Several recent experiments have demonstrated that when molecules form aggregates, the non-radiative decay rate does not increase significantly and may even decrease, despite a substantial reduction in the energy gap compared to isolated monomers in dilute solutions [139–141]. This observation contradicts conventional predictions of energy gap law and has drawn attention for its potential in developing near-infrared (NIR) emitting systems. Traditional NIR-emitting materials generally suffer from low emission efficiency due to rapid non-radiative decay caused by their small energy gaps.

The underlying mechanism behind this unusual behavior is thought to differ from AIE, as the involved molecules are planar and rigid, and thus should be unaffected by steric hindrance [139, 140]. The original work proposed that the exciton delocalization reduces electron-vibration coupling [139], such that when an exciton delocalizes across N molecules, the reorganization energy λ scales as λ/N, leading to a lower non-radiative decay rate. Subsequent theoretical work further refined this model, providing an analytical expression describing the non-radiative decay rate from the lowest excited state as a function of N [118]. While these studies capture the main physics, it should be noted that the results only hold under strong excitonic coupling limit.

To illustrate, we analyze the PES of a dimer (Figure 11), where the vibrational modes of the two molecules are denoted q_1 and q_2. At $J = 0$ (the first column), the electronic states (ϕ_1, ϕ_2) are fully localized, with each PES representing the excitation of a single molecule. As J increases (the second and third columns), the PESs split, and the two minima of the lower PES shift toward a central point. Under strong excitonic coupling limit (the fourth column), the electronic states become fully delocalized, forming states $\frac{\sqrt{2}}{2}(\phi_1 \pm \phi_2)$, which create two well-separated PESs. The lower PES becomes harmonic with a single minimum, and normal modes $q_\pm = \frac{\sqrt{2}}{2}(q_1 \pm q_2)$. Only in this condition, vibronic coupling between the two adiabatic PESs is negligible, allowing us to focus on the lowest surface alone. The displacement of the lower PES along q_+ is $D/\sqrt{2}$ and along q_- is 0, resulting in electron-vibration coupling strength $g_+ = g/\sqrt{2}$, $g_- = 0$, and reorganization energies $\lambda_+ = \lambda/2$, $\lambda_- = 0$. Similarly, for N molecules in the strong excitonic coupling limit, only the fully symmetric vibrational mode $q_+ = \frac{1}{\sqrt{N}} \sum_n q_n$ has displacement, reduced to $1/\sqrt{N}$, and so does the electron-vibration coupling.

Beyond the strong excitonic coupling limit, vibronic effects are substantial, especially with small energy gaps between the two adiabatic PESs. In this intermediate regime, the exciton is neither fully localized nor fully delocalized, requiring a non-perturbative approach. We applied the TD-DMRG method described previously to achieve near-exact calculations [49]. We start with a J-type dimer model where each molecule has two effective vibrational modes of frequency $\omega = 1400$ cm^{-1}: one promoting mode with non-adiabatic coupling constant F and one accepting mode with Huang–Rhys factor S. The adiabatic excitation energy is $E_{\mathrm{ad}} = 10\omega$. We calculated the ratio of the dimer's non-radiative decay rate $k_{\mathrm{nr}}^{\mathrm{agg}}$ to that of a single molecule $k_{\mathrm{nr}}^{\mathrm{mono}}$ under varying Huang–Rhys factors and excitonic coupling strengths. Figure 12A shows that as J increases, $k_{\mathrm{nr}}^{\mathrm{agg}}/k_{\mathrm{nr}}^{\mathrm{mono}}$ initially decreases, then rises. The magnitude of the reduction in $k_{\mathrm{nr}}^{\mathrm{agg}}/k_{\mathrm{nr}}^{\mathrm{mono}}$ grows with the Huang–Rhys factor. Inspired by single-molecule theory, we identified reorganization energy and the energy gap of the dimer as primary factors affecting the non-radiative decay rate. Using the vibrational distortion field (VDF) introduced in Section 2, we calculated the effective reorganization energy $\tilde{\lambda} = \sum_{l,r} \omega_l D_l(r)^2$. We also calculated the energy of the lowest vibronic state to get the energy gap. The reorganization energy and energy gap are plotted in Figure 12B. For small J/λ, $\tilde{\lambda}$ decreases rapidly while the energy gap ΔE declines slowly. Here, the reduction in reorganization energy dominates, causing a reduction in $k_{\mathrm{nr}}^{\mathrm{agg}}/k_{\mathrm{nr}}^{\mathrm{mono}}$. As J/λ increases further, $\tilde{\lambda}$ converges to a constant $\lambda/2$, while the energy gap decreases linearly, that is, $\Delta E = kJ, k = -1$, leading to an increase in $k_{\mathrm{nr}}^{\mathrm{agg}}/k_{\mathrm{nr}}^{\mathrm{mono}}$. Since the energy gap decreases monotonically with J, an anomalous energy gap law appears in the small-J region and then returns to the normal energy gap law at larger J values. We also observed similar non-monotonic trends in dimers with multiple vibrational modes and in H-type dimers [49].

Since the reduction in effective electron-vibration coupling strength is related to exciton delocalization length—increasing the delocalization length reduces the electron-vibration coupling, we further investigated the non-radiative decay rates dependence on aggregate size and dimensionality. For a 1D molecular chain ($N = 20$) and a 2D planar cluster ($N = 6 \times 6$), we calculated $k_{\mathrm{nr}}^{\mathrm{agg}}/k_{\mathrm{nr}}^{\mathrm{mono}}$ as J varied. Figure 12C shows that non-monotonic behavior persists for both the 1D chain and 2D cluster. Additionally, as J increases, the magnitude of reduction in $k_{\mathrm{nr}}^{\mathrm{agg}}/k_{\mathrm{nr}}^{\mathrm{mono}}$ for the 1D chain exceeds that of dimers, while the 2D cluster exhibits even greater changes, suggesting that the reduction in $k_{\mathrm{nr}}^{\mathrm{agg}}/k_{\mathrm{nr}}^{\mathrm{mono}}$ strengthens with increased system size and dimensionality. This can be qualitatively attributed to

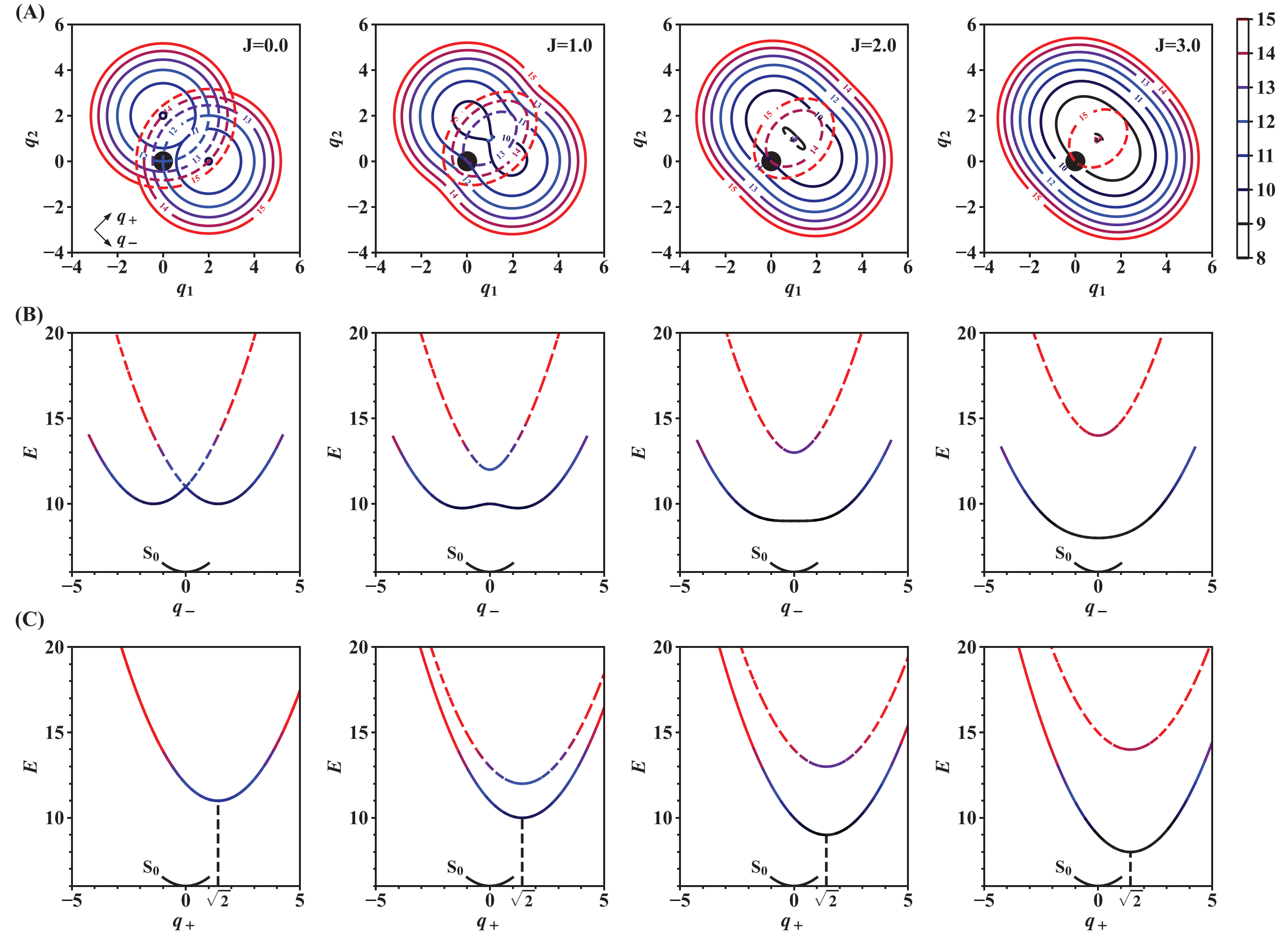

FIGURE 11 | The potential energy surfaces (PES) of a dimer with excitonic coupling. (A) Contours of two excited state PESs for $J = 0$, 1, 2, and 3 (using $\omega = 1$ as the unit). Solid and dashed contours represent the lower and upper adiabatic excited states, respectively. The black circle indicates the ground state PES at equilibrium geometry $q_1 = q_2 = 0$. The displacement of the two local excited states relative to the ground state is 2 along q_1 and q_2, respectively, corresponding to a Huang-Rhys factor S = 4. (B) The potential energy curve as a function of $q_- = \frac{\sqrt{2}}{2}(q_1 - q_2)$, with $q_+ = \frac{\sqrt{2}}{2}(q_1 + q_2)$, fixed at $\sqrt{2}$. (C) The potential energy curve as a function of q_+, with q_- fixed at 0. The adiabatic excitation energy of the local excited state is set to 10. The ground state PES is elevated to be visible.

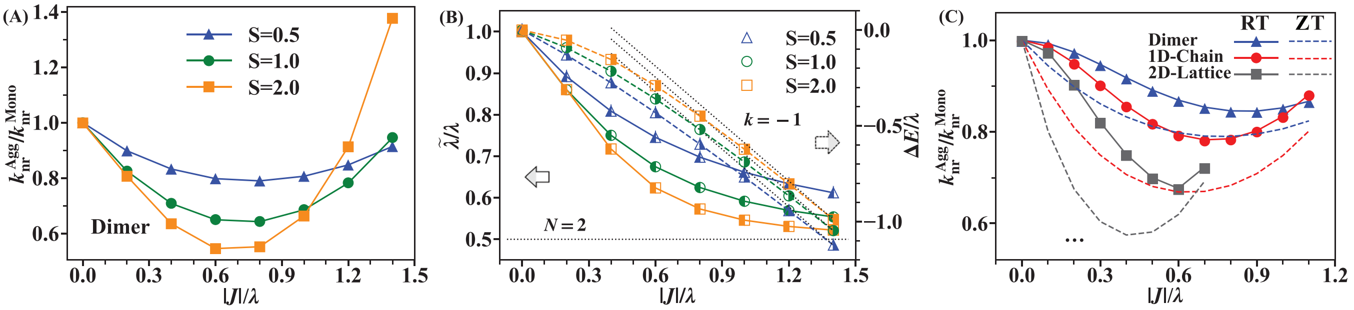

FIGURE 12 | (A) Non-radiative decay rate of a dimer ($N = 2$) relative to that of a monomer $k_{\mathrm{nr}}^{\mathrm{agg}}/k_{\mathrm{nr}}^{\mathrm{mono}}$ in systems with varying electron-vibration couplings S and excitonic couplings J, simulated using the time-dependent density matrix renormalization group (TD-DMRG) method. (B) Effective reorganization energy $\tilde{\lambda}$ (solid curves, left y-axis) and the energy gap narrowing ΔE (dashed curves, right y-axis) as a function of excitonic coupling J. The black dotted line represents the analytical solution $\tilde{\lambda} = \lambda/2$, $\Delta E/J = -1$ in the strong excitonic coupling limit. (C) $k_{\mathrm{nr}}^{\mathrm{agg}}/k_{\mathrm{nr}}^{\mathrm{mono}}$ at 0 and 300 K for the dimer (blue), one-dimensional chain ($N = 20$, red), and two-dimensional planar cluster ($N = 6 \times 6$, black). Figure adapted from Ref. 52.

variations in exciton delocalization length: as shown by the VDF in Figure 3, 2D stacking results in greater delocalization than the 1D chain at the same J, further reducing electron-vibration coupling. Additionally, at 300 K, the exciton delocalization length decreases due to enhanced dynamic disorder, which leads to a smaller reduction in $k_{\mathrm{nr}}^{\mathrm{agg}}/k_{\mathrm{nr}}^{\mathrm{mono}}$ compared to 0 K (Figure 12C).

In summary, our calculations quantitatively explain the experimentally observed reductions in non-radiative decay rates from monomers to aggregates due to excitonic coupling effects. We further demonstrate that maximizing exciton coupling J is not always beneficial; rather, an optimal $J \approx \lambda/2$ exists, where the non-radiative decay rate is minimized. If J is larger than this value, the non-radiative decay rate reverts to behavior predicted by the normal energy gap law. This insight suggests that photoluminescent quantum yield can be enhanced by optimizing molecular stacking to tune excitonic coupling J to this optimal value.

5 | Conclusions

To conclude, we reported our recent progresses toward understanding the intermolecular coupling and CT effects on the optical processes in molecular aggregates. ECL is an important concept to measure the exciton delocalization range. For J-aggregate, the superradiance efficiency is proportional to this length. There have been a number of definitions of coherence length in literature, none of which could correlate with superradiance efficiency. By virtue of sum-rule for oscillator strength, we suggested a unified definition and based on that, we have made theoretical prediction of novel non-monotomic temperature dependence for the excited state lifetime in the H–J mixed aggregate. Although, it was known that CT can alter the nature of the lowest-lying excited state for aggregate through intensity borrowing, we proposed a working principle for molecular design as how to obtain light-emitting and carrier transporting materials. And finally, we investigated the excitonic coupling effect on the non-radiative decay rate. We found that conventional energy gap law fails for aggregate due to the reduced reorganization energy on top of the red-shift in emission. These two opposing effects combine to demonstrate an optimal J to minimize non-radiative decay rate. It should be noted that a number of novel aggregation-induced phenomena appeared in recent years and remained mysterious or controversial. There lacks unified theoretical descriptions for the electronic structure and quantum dynamics. This is a formidable task remaining challenging for theoretical and computational chemistry.

Acknowledgments

This work was supported by the National Natural Science Foundation of China (grant nos. T2350009 and 22433007), the Guangdong Provincial Natural Science Foundation (grant no. 2024A1515011185), the Shenzhen City Pengcheng Peacock Talent Program, and Shenzhen Science and Technology Program (no. KQTD20240729102028011). Jiajun Ren is supported by the National Natural Science Foundation of China (grant nos. 22273005 and 22422301).

Conflicts of Interest

The authors declare they have no conflicts of interest.

References

1. J. Luo, Z. Xie, J. W. Lam, et al., "Aggregation-Induced Emission of 1-Methyl-1,2,3,4,5-Pentaphenylsilole," *Chemical Communications* no. 18 (2001): 1740–1741.

2. J. L. Brédas, J. Cornil, D. Beljonne, D. A. Dos Santos, and Z. Shuai, "Excited-State Electronic Structure of Conjugated Oligomers and Polymers: A Quantum-Chemical Approach to Optical Phenomena," *Accounts of Chemical Research* 32, no. 3 (1999): 267–276.

3. M. Kasha, "Energy Transfer Mechanisms and the Molecular Exciton Model for Molecular Aggregates," *Radiation Research* 20, no. 1 (1963): 55–70.

4. W. P. Su, J. R. Schrieffer, and A. J. Heeger, "Solitons in Polyacetylene," *Physical Review Letters* 42, no. 25 (1979): 1698.

5. N. J. Hestand and F. C. Spano, "Molecular Aggregate Photophysics Beyond the Kasha Model: Novel Design Principles for Organic Materials," *Accounts of Chemical Research* 50, no. 2 (2017): 341–350.

6. N. J. Hestand and F. C. Spano, "Expanded Theory of H- and J-Molecular Aggregates: The Effects of Vibronic Coupling and Intermolecular Charge Transfer," *Chemical Reviews* 118, no. 15 (2018): 7069–7163.

7. Q. Sun, J. Ren, T. Jiang, Q. Peng, Q. Ou, and Z. Shuai, "Intermolecular Charge-Transfer-Induced Strong Optical Emission From Herringbone H-Aggregates," *Nano Letters* 21, no. 12 (2021): 5394–5400.

8. S. Fratini, S. Ciuchi, D. Mayou, G. T. De Laissardière, and A. Troisi, "A Map of High-Mobility Molecular Semiconductors," *Nature Materials* 16, no. 10 (2017): 998–1002.

9. W. Li, Q. Peng, Y. Xie, T. Zhang, and Z. Shuai, "Effect of Intermolecular Excited-State Interaction on Vibrationally Resolved Optical Spectra in Organic Molecular Aggregates," *Acta Chimica Sinica* 74, no. 11 (2016): 902.

10. M. Kasha, H. R. Rawls, and M. Ashraf El-Bayoumi, "The Exciton Model in Molecular Spectroscopy," *Pure and Applied Chemistry VIIIth* 11, no. 34 (1965): 371–392.

11. O. Ostroverkhova, "Organic Optoelectronic Materials: Mechanisms and Applications," *Chemical Reviews* 116, no. 22 (2016): 13279–13412.

12. O. P. Dimitriev, "Dynamics of Excitons in Conjugated Molecules and Organic Semiconductor Systems," *Chemical Reviews* 122, no. 9 (2022): 8487–8593.

13. C. Wang, H. Dong, W. Hu, Y. Liu, and D. Zhu, "Semiconducting π-Conjugated Systems in Field-Effect Transistors: A Material Odyssey of Organic Electronics," *Chemical Reviews* 112, no. 4 (2012): 2208–2267.

14. N. J. Hestand and F. C. Spano, "Expanded Theory of H-and J-Molecular Aggregates: The Effects of Vibronic Coupling and Intermolecular Charge Transfer," *Chemical Reviews* 118, no. 15 (2018): 7069–7163.

15. R. M. Clegg, "Förster Resonance Energy Transfer FRET What Is It, Why Do It, and How It's Done," *Laboratory Techniques in Biochemistry and Molecular Biology* 33 (2009): 1–57.

16. I. L. Medintz and N. Hildebrandt, *FRET-Förster Resonance Energy Transfer: From Theory to Applications* (John Wiley & Sons, 2013).

17. T. Förster, *Mechanisms of Energy Transfer*, Vol. 22 (Waltham, MA, USA: Elsevier, 1967), 61–80.

18. A. Davydov, *Theory of Molecular Excitons* (Springer, 2013).

19. V. Agranovich, *Excitations in Organic Solids*, Vol. 142 (International Monographs on Physics, 2009).

20. V. Czikklely, H. Forsterling, and H. Kuhn, "Extended Dipole Model for Aggregates of Dye Molecules," *Chemical Physics Letters* 6, no. 3 (1970): 207–210.

21. B. P. Krueger, G. D. Scholes, and G. R. Fleming, "Calculation of Couplings and Energy-Transfer Pathways Between the Pigments of LH2 by the Ab Initio Transition Density Cube Method," *The Journal of Physical Chemistry B* 102, no. 27 (1998): 5378–5386.

22. M. Rodriguez-Mayorga, X. Blase, I. Duchemin, and G. DAvino, "From Many-Body Ab Initio to Effective Excitonic Models: a Versatile Mapping

Approach Including Environmental Embedding Effects," *Journal of Chemical Theory and Computation* 20 (2024): 8675–8688.

23. T. L. Jansen, "Computational Spectroscopy of Complex Systems," *The Journal of Chemical Physics* 155, no. 17 (2021): 170901.

24. W. Liang, Y. C. Wang, S. Feng, and Y. Zhao, "Modeling the Photophysical Processes of Organic Molecular Aggregates With Inclusion of Intermolecular Interactions and Vibronic Couplings," *Exploring Chemical Concepts Through Theory and Computation* 379 (2024): Chapter 15.

25. T. Kobayashi, *J-aggregates*, Vol. 2 (World Scientific, 2012).

26. J. Knoester and V. M. Agranovich, "Frenkel and Charge-Transfer Excitons in Organic Solids," *Thin Films and Nanostructures* 31 (2003): 1–96.

27. M. Hecht and F. Wurthner, "Supramolecularly Engineered J-Aggregates Based on Perylene Bisimide Dyes," *Accounts of Chemical Research* 54, no. 3 (2020): 642–653.

28. F. Würthner, T. E. Kaiser, and C. R. Saha-Möller, "J-Aggregates: From Serendipitous Discovery to Supramolecular Engineering of Functional Dye Materials," *Angewandte Chemie International Edition* 50, no. 15 (2011): 3376–3410.

29. J. R. Tischler, M. S. Bradley, V. Bulovic, J. H. Song, and A. Nurmikko, "Strong Coupling in a Microcavity LED," *Physical Review Letters* 95, no. 3 (2005): 036401.

30. B. J. Walker, A. Dorn, V. Bulovic, and M. G. Bawendi, "Color-Selective Photocurrent Enhancement in Coupled J-Aggregate/Nanowires Formed in Solution," *Nano Letters* 11, no. 7 (2011): 2655–2659.

31. G. D. Scholes, G. R. Fleming, L. X. Chen, et al., "Using Coherence to Enhance Function in Chemical and Biophysical Systems," *Nature* 543, no. 7647 (2017): 647–656.

32. F. C. Spano, J. Clark, C. Silva, and R. H. Friend, "Determining Exciton Coherence From the Photoluminescence Spectral Line Shape in Poly(3-Hexylthiophene) Thin Films," *The Journal of Chemical Physics* 130, no. 7 (2009): 074904.

33. Z. Xie, D. Liu, C. Gao, H. Dong, and W. Hu, "High-Mobility Emissive Organic Semiconductors: An Emerging Class of Multifunctional Materials," *Nature Reviews Materials* 9, no. 12 (2024): 1–3.

34. J. Gierschner, L. Luer, B. Milián-Medina, D. Oelkrug, and H. J. Egelhaaf, "Highly Emissive H-Aggregates or Aggregation-Induced Emission Quenching? The Photophysics of All-Trans Para-Distyrylbenzene," *The Journal of Physical Chemistry Letters* 4, no. 16 (2013): 2686–2697.

35. H. Fidder, J. Knoester, and D. A. Wiersma, "Superradiant Emission and Optical Dephasing in J-Aggregates," *Chemical Physics Letters* 171, no. 5–6 (1990): 529–536.

36. F. C. Spano, J. R. Kuklinski, and S. Mukamel, "Temperature-Dependent Superradiant Decay of Excitons in Small Aggregates," *Physical Review Letters* 65, no. 2 (1990): 211.

37. S. K. Saikin, A. Eisfeld, S. Valleau, and A. Aspuru-Guzik, "Photonics Meets Excitonics: Natural and Artificial Molecular Aggregates," *Nanophotonics* 2, no. 1 (2013): 21–38.

38. T. Brixner, R. Hildner, J. Köhler, C. Lambert, and F. Würthner, "Exciton Transport in Molecular Aggregates—From Natural Antennas to Synthetic Chromophore Systems," *Advanced Energy Materials* 7, no. 16 (2017): 1700236.

39. F. C. Spano, "Excitons in Conjugated Oligomer Aggregates, Films, and Crystals," *Annual Review of Physical Chemistry* 57, no. 1 (2006): 217–243.

40. C. J. Bardeen, "The Structure and Dynamics of Molecular Excitons," *Annual Review of Physical Chemistry* 65, no. 1 (2014): 127–148.

41. Q. Peng and Z. Shuai, "Molecular mechanism of aggregation-induced emission," *Aggregate* 2, no. 5 (2021): e91.

42. K. H. Park, W. Kim, J. Yang, and D. Kim, "Excited-State Structural Relaxation and Exciton Delocalization Dynamics in Linear and Cyclic π-Conjugated Oligothiophenes," *Chemical Society Reviews* 47, no. 12 (2018): 4279–4294.

43. R. Binder, D. Lauvergnat, and I. Burghardt, "Conformational Dynamics Guides Coherent Exciton Migration in Conjugated Polymer Materials: First-Principles Quantum Dynamical Study," *Physical Review Letters* 120, no. 22 (2018): 227401.

44. M. Deutsch, S. Wirsing, D. Kaiser, R. Fink, P. Tegeder, and B. Engels, "Geometry Relaxation-Mediated Localization and Delocalization of Excitons in Organic Semiconductors: a Quantum Chemical Study," *The Journal of Chemical Physics* 153, no. 22 (2020): 224104.

45. M. Schröter, S. D. Ivanov, J. Schulze, et al., "Exciton–Vibrational Coupling in the Dynamics and Spectroscopy of Frenkel Excitons in Molecular Aggregates," *Physics Reports* 567 (2015): 1–78.

46. J. Ren, Z. Shuai, and G. Kin-Lic Chan, "Time-Dependent Density Matrix Renormalization Group Algorithms for Nearly Exact Absorption and Fluorescence Spectra of Molecular Aggregates at both Zero and Finite Temperature," *Journal of Chemical Theory and Computation* 14, no. 10 (2018): 5027–5039.

47. T. Jiang, W. Li, J. Ren, and Z. Shuai, "Finite Temperature Dynamical Density Matrix Renormalization Group for Spectroscopy in Frequency Domain," *The Journal of Physical Chemistry Letters* 11, no. 10 (2020): 3761–3768.

48. W. Li, J. Ren, and Z. Shuai, "A General Charge Transport Picture for Organic Semiconductors With Nonlocal Electron–Phonon Couplings," *Nature Communications* 12, no. 1 (2021): 4260.

49. Y. Wang, J. Ren, and Z. Shuai, "Minimizing Non-Radiative Decay in Molecular Aggregates Through Control of Excitonic Coupling," *Nature Communications* 14, no. 1 (2023): 5056.

50. T. Holstein, "Studies of Polaron Motion," *Annals of Physics* 8, no. 3 (1959): 325–342.

51. T. Holstein, "Studies of Polaron Motion," *Annals of Physics* 8, no. 3 (1959): 343–389.

52. R. Ghosh and F. C. Spano, "Excitons and Polarons in Organic Materials," *Accounts of Chemical Research* 53, no. 10 (2020): 2201–2211.

53. F. C. Spano and H. Yamagata, "Vibronic Coupling in J-aggregates and Beyond: a Direct Means of Determining the Exciton Coherence Length From the Photoluminescence Spectrum," *The Journal of Physical Chemistry B* 115, no. 18 (2011): 5133–5143.

54. T. Meier, Y. Zhao, V. Chernyak, and S. Mukamel, "Polarons, Localization, and Excitonic Coherence in Superradiance of Biological Antenna Complexes," *The Journal of Chemical Physics* 107, no. 10 (1997): 3876–3893.

55. C. Smyth, F. Fassioli, and G. D. Scholes, "Measures and Implications of Electronic Coherence in Photosynthetic Light-harvesting," *Philosophical Transactions of the Royal Society Series A* 370 (2012): 3728–3749.

56. J. D. Schultz, J. L. Yuly, E. A. Arsenault, et al., "Coherence in Chemistry: Foundations and Frontiers," *Chemical Reviews* 124 (2024): 11641–11766.

57. C. C. Jumper, S. R. Rather, S. Wang, and G. D. Scholes, "From Coherent to Vibronic Light Harvesting in Photosynthesis," *Current Opinion in Chemical Biology* 47 (2018): 39–46.

58. T. Wang and W. L. Chan, "Dynamical Localization Limiting the Coherent Transport Range of Excitons in Organic Crystals," *The Journal of Physical Chemistry Letters* 5, no. 11 (2014): 1812–1818.

59. W. Popp, D. Brey, R. Binder, and I. Burghardt, "Quantum Dynamics of Exciton Transport and Dissociation in Multichromophoric Systems," *Annual Review of Physical Chemistry* 72, no. 1 (2021): 591–616.

60. S. H. Lim, T. G. Bjorklund, F. C. Spano, and C. J. Bardeen, "Exciton Delocalization and Superradiance in Tetracene Thin Films and Nanoaggregates," *Physical Review Letters* 92, no. 10 (2004): 107402.

61. D. H. Arias, K. W. Stone, S. M. Vlaming, et al., "Thermally-Limited Exciton Delocalization in Superradiant Molecular Aggregates," *The Journal of Physical Chemistry B* 117, no. 16 (2013): 4553–4559.

62. T. Jiang, J. Ren, and Z. Shuai, "Unified Definition of Exciton Coherence Length for Exciton–Phonon Coupled Molecular Aggregates," *Journal of Physical Chemistry Letters* 14, no. 19 (2023): 4541–4547.

63. S. Tretiak and S. Mukamel, "Density Matrix Analysis and Simulation of Electronic Excitations in Conjugated and Aggregated Molecules," *Chemical Reviews* 102, no. 9 (2002): 3171–3212.

64. J. Yuen-Zhou, J. J. Krich, M. Mohseni, and A. Aspuru-Guzik, "Quantum state and Process Tomography of Energy Transfer Systems via Ultrafast Spectroscopy," *Proceedings of the National Academy of Sciences* 108, no. 43 (2011): 17615–17620.

65. J. Ren, W. Li, T. Jiang, Y. Wang, and Z. Shuai, "Time-dependent Density Matrix Renormalization Group Method for Quantum Dynamics in Complex Systems," *Wiley Interdisciplinary Reviews: Computational Molecular Science* 12, no. 6 (2022): e1614.

66. J. M. Moix, Y. Zhao, and J. Cao, "Equilibrium-reduced Density Matrix Formulation: Influence of Noise, Disorder, and Temperature on Localization in Excitonic Systems," *Physical Review B* 85, no. 11 (2012): 115412.

67. D. J. Thouless, "Electrons in Disordered Systems and the Theory of Localization," *Physics Reports* 13, no. 3 (1974): 93–142.

68. V. Novoderezhkin, R. Monshouwer, and V. R. Grondelle, "Exciton (de) Localization in the LH2 Antenna of Rhodobacter Sphaeroides as Revealed by Relative Difference Absorption Measurements of the LH2 Antenna and the B820 Subunit," *The Journal of Physical Chemistry B* 103, no. 47 (1999): 10540–10548.

69. R. Jimenez, S. N. Dikshit, S. E. Bradforth, and G. R. Fleming, "Electronic Excitation Transfer in the LH2 Complex of Rhodobacter Sphaeroides," *The Journal of Physical Chemistry* 100, no. 16 (1996): 6825–6834.

70. H. Fidder, J. Knoester, and D. A. Wiersma, "Optical Properties of Disordered Molecular Aggregates: A Numerical Study," *The Journal of Chemical Physics* 95, no. 11 (1991): 7880–7890.

71. A. Ishizaki and G. R. Fleming, "Quantum Superpositions in Photosynthetic Light Harvesting: Delocalization and Entanglement," *New Journal of Physics* 12, no. 5 (2010): 055004.

72. H. Hossein-Nejad, C. Curutchet, A. Kubica, and G. D. Scholes, "Delocalization-Enhanced Long-Range Energy Transfer Between Cryptophyte Algae PE545 Antenna Proteins," *The Journal of Physical Chemistry B* 115, no. 18 (2011): 5243–5253.

73. K. Zyczkowski, P. Horodecki, A. Sanpera, and M. Lewenstein, "Volume of the Set of Separable States," *Physical Review A* 58, no. 2 (1998): 883.

74. A. Eisfeld, S. Vlaming, V. Malyshev, and J. Knoester, "Excitons in Molecular Aggregates With Lévy-Type Disorder: Anomalous Localization and Exchange Broadening of Optical Spectra," *Physical Review Letters* 105, no. 13 (2010): 137402.

75. G. D. Scholes, "Limits of Exciton Delocalization in Molecular Aggregates," *Faraday Discussions* 221 (2020): 265–280.

76. O. Kühn and V. Sundström, "Pump–Probe Spectroscopy of Dissipative Energy Transfer Dynamics in Photosynthetic Antenna Complexes: A Density Matrix Approach," *The Journal of Chemical Physics* 107, no. 11 (1997): 4154–4164.

77. F. C. Spano, S. C. Meskers, E. Hennebicq, and D. Beljonne, "Using Circularly Polarized Luminescence to Probe Exciton Coherence in Disordered Helical Aggregates," *The Journal of Chemical Physics* 129, no. 2 (2008): 024704.

78. M. Dahlbom, T. Pullerits, S. Mukamel, and V. Sundström, "Exciton Delocalization in the B850 Light-Harvesting Complex: Comparison of Different Measures," *The Journal of Physical Chemistry B* 105, no. 23 (2001): 5515–5524.

79. L. Book, A. Ostafin, N. Ponomarenko, J. Norris, and N. Scherer, "Exciton Delocalization and Initial Dephasing Dynamics of Purple Bacterial LH2," *The Journal of Physical Chemistry B* 104, no. 34 (2000): 8295–8307.

80. L. E. H. Rodríguez and A. A. Kananenka, "A Systematic Study of the Role of Dissipative Environment in Regulating Entanglement and Exciton Delocalization in the Fenna-Matthews-Olson Complex," *Arxiv* (2024): 2401.01534, https://doi.org/10.48550/arXiv.2401.01534.

81. Z. Sheng, T. Jiang, W. Li, and Z. Shuai, "TD-DMRG Study of Exciton Dynamics With both Thermal and Static Disorders for Fenna-Matthews-Olson Complex," *Journal of Chemical Theory and Computation* 20 (2024): 6470–6484.

82. M. Sarovar, A. Ishizaki, G. R. Fleming, and K. B. Whaley, "Quantum Entanglement in Photosynthetic Light-harvesting Complexes," *Nature Physics* 6, no. 6 (2010): 462–467.

83. D. A. Meyer and N. R. Wallach, "Global Entanglement in Multiparticle Systems," *Journal of Mathematical Physics* 43, no. 9 (2002): 4273–4278.

84. T. Scholak, D. F. Melo, T. Wellens, F. Mintert, and A. Buchleitner, "Efficient and Coherent Excitation Transfer Across Disordered Molecular Networks," *Physical Review EStatistical, Nonlinear, and Soft Matter Physics* 83, no. 2 (2011): 021912.

85. W. Wu and G. D. Scholes, "Foundations of Quantum Information for Physical Chemistry," *Journal of Physical Chemistry Letters* 15, no. 15 (2024): 4056–4069.

86. J. B. Trebbia, Q. Deplano, P. Tamarat, and B. Lounis, "Tailoring the Superradiant and Subradiant Nature of Two Coherently Coupled Quantum Emitters," *Nature Communications* 13, no. 1 (2022): 1–9.

87. Y. Zhang, Y. Luo, Y. Zhang, et al., "Visualizing Coherent Intermolecular Dipole–Dipole Coupling in Real Space," *Nature* 531, no. 7596 (2016): 623–627.

88. Y. Wu, Y. Zhu, C. Yao, et al., "Recent Advances in Small-Molecule Fluorescent Photoswitches With Photochromism in Diverse States," *Journal of Materials Chemistry C* 11, no. 44 (2023): 15393–15411.

89. W. Li, J. Ren, and Z. Shuai, "Numerical Assessment for Accuracy and GPU Acceleration of TD-DMRG Time Evolution Schemes," *The Journal of Chemical Physics* 152, no. 2 (2020): 024127.

90. T. Jiang, J. Ren, and Z. Shuai, "Chebyshev Matrix Product States With Canonical Orthogonalization for Spectral Functions of Many-Body Systems," *The Journal of Physical Chemistry Letters* 12, no. 38 (2021): 9344–9352.

91. C. Chuang, D. I. Bennett, J. R. Caram, A. Aspuru-Guzik, M. G. Bawendi, and J. Cao, "Generalized Kasha's Model: T-Dependent Spectroscopy Reveals Short-Range Structures of 2D Excitonic Systems," *Chemistry* 5, no. 12 (2019): 3135–3150.

92. A. E. Sifain, F. Fassioli, and G. D. Scholes, "Toward Witnessing Molecular Exciton Entanglement From Spectroscopy," *Physical Review A* 104, no. 4 (2021): 042416.

93. F. C. Spano, "Temperature Dependent Exciton Emission From Herringbone Aggregates of Conjugated Oligomers," *The Journal of Chemical Physics* 120, no. 16 (2004): 7643–7658.

94. F. Gao, Y. Zhao, and W. Liang, "Vibronic Spectra of Perylene Bisimide Oligomers: Effects of Intermolecular Charge-Transfer Excitation and Conformational Flexibility," *The Journal of Physical Chemistry B* 115, no. 12 (2011): 2699–2708.

95. F. Gao, W. Z. Liang, and Y. Zhao, "Vibrationally Resolved Absorption and Emission Spectra of Rubrene Multichromophores: Temperature and Aggregation Effects," *The Journal of Physical Chemistry A* 113, no. 46 (2009): 12847–12856.

96. N. J. Hestand and F. C. Spano, "Interference Between Coulombic and CT-Mediated Couplings in Molecular Aggregates: H- to J-Aggregate Transformation in Perylene-Based Π-Stacks," *The Journal of Chemical Physics* 143, no. 24 (2015): 244707.

97. H. Yamagata, C. M. Pochas, and F. C. Spano, "Designing J- and H-Aggregates Through Wave Function Overlap Engineering: Applications to Poly(3-hexylthiophene)," *Journal of Physical Chemistry B* 116, no. 49 (2012): 14494–14503.

98. N. J. Hestand, R. V. Kazantsev, A. S. Weingarten, L. C. Palmer, S. I. Stupp, and F. C. Spano, "Extended-Charge-Transfer Excitons in Crystalline Supramolecular Photocatalytic Scaffolds," *Journal of the American Chemical Society* 138, no. 36 (2016): 11762–11774.

99. Q. Sun, T. Jiang, Q. Ou, Q. Peng, and Z. Shuai, "Influence of Intermolecular Packing on Light Emitting Efficiency and Carrier-Mobility of Organic Semiconductors: Theoretical Descriptor for Molecular Design," *Advanced Optical Materials* 11, no. 5 (2023): 2202621.

100. Z. Qin, H. Gao, H. Dong, and W. Hu, "Organic Light-Emitting Transistors Entering a New Development Stage," *Advanced Materials* 33, no. 31 (2021): 2007149.

101. K. Carter-Fenk, K. U. Lao, K. Y. Liu, and J. M. Herbert, "Accurate and Efficient Ab Initio Calculations for Supramolecular Complexes: Symmetry-Adapted Perturbation Theory With Many-Body Dispersion," *The Journal of Physical Chemistry Letters* 10, no. 11 (2019): 2706–2714.

102. P. Petelenz, M. Snamina, and G. Mazur, "Charge-Transfer States in Pentacene: Dimer Versus Crystal," *The Journal of Physical Chemistry C* 119, no. 25 (2015): 14338–14342.

103. J. Liu, H. Zhang, H. Dong, et al., "High Mobility Emissive Organic Semiconductor," *Nature Communications* 6, no. 1 (2015): 10032.

104. J. Li, K. Zhou, J. Liu, et al., "Aromatic Extension at 2,6-Positions of Anthracene Toward an Elegant Strategy for Organic Semiconductors With Efficient Charge Transport and Strong Solid State Emission," *Journal of the American Chemical Society* 139, no. 48 (2017): 17261–17264.

105. J. E. Subotnik, S. Yeganeh, R. J. Cave, and M. A. Ratner, "Constructing Diabatic States From Adiabatic States: Extending Generalized Mulliken–Hush to Multiple Charge Centers With Boys Localization," *Journal of Chemical Physics* 129, no. 24 (2008): 244101.

106. J. Liu, W. Zhu, K. Zhou, et al., "Pyridyl-substituted Anthracene Derivatives With Solid-State Emission and Charge Transport Properties," *Journal of Materials Chemistry C* 4, (2016): 3621–3627.

107. R. Katoh, K. Suzuki, A. Furube, M. Kotani, and K. Tokumaru, "Fluorescence Quantum Yield of Aromatic Hydrocarbon Crystals," *Journal of Physical Chemistry C* 113, no. 7 (2009): 2961–2965.

108. M. Nakano, H. Mori, S. Shinamura, and K. Takimiya, "Naphtho[2,3-b:6,7-b]Dichalcogenophenes: Syntheses, Characterizations, and Chalcogene Atom Effects on Organic Field-Effect Transistor and Organic Photovoltaic Devices," *Chemistry of Materials* 24, no. 1 (2012): 190–198.

109. C. Du, Y. Guo, Y. Liu, et al., "Anthra[2,3-b]Benzo[d]Thiophene: An Air-Stable Asymmetric Organic Semiconductor With High Mobility at Room Temperature," *Chemistry of Materials* 20, no. 13 (2008): 4188–4190.

110. J. G. Laquindanum, H. E. Katz, and A. J. Lovinger, "Synthesis, Morphology, and Field-Effect Mobility of Anthradithiophenes," *Journal of the American Chemical Society* 120, no. 4 (1998): 664–672.

111. T. Yamamoto and K. Takimiya, "Facile Synthesis of Highly pi-Extended Heteroarenes, Dinaphtho[2,3-b:2′,3′-f]Chalcogenopheno[3,2b]Chalcogenophenes, and Their Application to Field-Effect Transistors," *Journal of the American Chemical Society* 129, no. 8 (2007): 2224–2225.

112. T. Mori, T. Nishimura, T. Yamamoto, et al., "Consecutive Thiophene-Annulation Approach to π-Extended Thienoacene-Based Organic Semiconductors With [1]Benzothieno[3,2-b][1]benzothiophene (BTBT) Substructure," *Journal of the American Chemical Society* 135 (2013): 13900.

113. Q. Wu, T. Zhang, Q. Peng, D. Wang, and Z. Shuai, "Aggregation Induced Blue-Shifted Emission—The Molecular Picture From a QM/MM Study," *Physical Chemistry Chemical Physics* 16, no. 12 (2014): 5545–5552.

114. T. Zhang, Y. Jiang, Y. Niu, D. Wang, Q. Peng, and Z. Shuai, "Aggregation Effects on the Optical Emission of 1,1,2,3,4,5-Hexaphenylsilole (HPS): A QM/MM Study," *The Journal of Physical Chemistry A* 118, no. 39 (2014): 9094–9104.

115. B. Scharf and U. Dinur, "Striking Dependence of the Rate of Electronic Radiationless Transitions on the Size of the Molecular System," *Chemical Physics Letters* 105, no. 1 (1984): 78–82.

116. A. Celestino and A. Eisfeld, "Tuning Nonradiative Lifetimes via Molecular Aggregation," *The Journal of Physical Chemistry A* 121, no. 32 (2017): 5948–5953.

117. W. Li, L. Zhu, Q. Shi, J. Ren, Q. Peng, and Z. Shuai, "Excitonic Coupling Effect on the Nonradiative Decay Rate in Molecular Aggregates: Formalism and Application," *Chemical Physics Letters* 683 (2017): 507–514.

118. A. Humeniuk, R. Mitric, and V. Bonacic-Koutecky, "Size Dependence of Non-Radiative Decay Rates in J-Aggregates," *The Journal of Physical Chemistry A* 124, no. 49 (2020): 10143–10151.

119. B. F. Curchod and T. J. Martínez, "Ab Initio Nonadiabatic Quantum Molecular Dynamics," *Chemical Reviews* 118, no. 7 (2018): 3305–3336.

120. R. Crespo-Otero and M. Barbatti, "Recent Advances and Perspectives on Nonadiabatic Mixed Quantum–Classical Dynamics," *Chemical Reviews* 118, no. 15 (2018): 7026–7068.

121. K. Huang and A. Rhys, "Theory of Light Absorption and Non-Radiative Transitions in F-Centres," *Proceedings of the Royal Society of London Series A Mathematical and Physical Sciences* 204, no. 1078 (1950): 406–423.

122. S. H. Lin, "Rate of Interconversion of Electronic and Vibrational Energy," *The Journal of Chemical Physics* 44, no. 10 (1966): 3759–3767.

123. S. Lin, C. Chang, K. Liang, et al., "Ultrafast Dynamics and Spectroscopy of Bacterial Photosynthetic Reaction Centers," *Advances in Chemical Physics* 121 (2002): 1–88.

124. R. Englman and J. Jortner, "The Energy Gap Law for Radiationless Transitions in Large Molecules," *Molecular Physics* 18, no. 2 (1970): 145–164.

125. S. H. Lin and R. Bersohn, "Effect of Partial Deuteration and Temperature on Triplet-State Lifetimes," *The Journal of Chemical Physics* 48, no. 6 (1968): 2732–2736.

126. M. Hayashi, A. Mebel, K. Liang, and S. Lin, "Ab Initio Calculations of Radiationless Transitions Between Excited and Ground Singlet Electronic States of Ethylene," *The Journal of Chemical Physics* 108, no. 5 (1998): 2044–2055.

127. Q. Peng, Y. Yi, Z. Shuai, and J. Shao, "Excited State Radiationless Decay Process With Duschinsky Rotation Effect: Formalism and Implementation," *The Journal of Chemical Physics* 126, no. 11 (2007): 114302.

128. Y. Niu, Q. Peng, and Z. Shuai, "Promoting-mode Free Formalism for Excited state Radiationless Decay Process With Duschinsky Rotation Effect," *Science in China Series B: Chemistry* 51, no. 12 (2008): 1153–1158.

129. Y. Niu, Q. Peng, C. Deng, X. Gao, and Z. Shuai, "Theory of Excited State Decays and Optical Spectra: Application to Polyatomic Molecules," *The Journal of Physical Chemistry A* 114, no. 30 (2010): 7817–7831.

130. Z. Shuai, "Thermal Vibration Correlation Function Formalism for Molecular Excited State Decay Rates," *Chinese Journal of Chemistry* 38, no. 11 (2020): 1223–1232.

131. Q. Peng, Y. Niu, Q. Shi, X. Gao, and Z. Shuai, "Correlation Function Formalism for Triplet Excited State Decay: Combined Spin–Orbit and Nonadiabatic Couplings," *Journal of Chemical Theory and Computation* 9, no. 2 (2013): 1132–1143.

132. Y. Niu, W. Li, Q. Peng, et al., "MOlecular MAterials Property Prediction Package (MOMAP) 1.0: A Software Package for Predicting the Luminescent Properties and Mobility of Organic Functional Materials," *Molecular Physics* 116, no. 7–8 (2018): 1078–1090.

133. S. G. Chiodo and T. Mineva, "Application of Vibrational Correlation Formalism to Internal Conversion Rate: Case Study of Cun (n = 3, 6, and 9) and H_2/Cu_3," *The Journal of Chemical Physics* 142, no. 11 (2015): 114311.

134. S. Banerjee, A. Baiardi, J. Bloino, and V. Barone, "Temperature Dependence of Radiative and Nonradiative Rates From Time-Dependent Correlation Function Methods," *Journal of Chemical Theory and Computation* 12, no. 2 (2016): 774–786.

135. A. Humeniuk, M. Bužancič, J. Hoche, et al., "Predicting Fluorescence Quantum Yields for Molecules in Solution: A Critical Assessment of the Harmonic Approximation and the Choice of the Lineshape Function," *The Journal of Chemical Physics* 152, no. 5 (2020): 054107.

136. J. Mei, N. L. Leung, R. T. Kwok, J. W. Lam, and B. Z. Tang, "Aggregation-Induced Emission: Together We Shine, United We Soar!," *Chemical Reviews* 115, no. 21 (2015): 11718–11940.

137. Y. Wang, J. Ren, and Z. Shuai, "Evaluating the Anharmonicity Contributions to the Molecular Excited State Internal Conversion Rates With Finite Temperature TD-DMRG," *The Journal of Chemical Physics* 154, no. 21 (2021): 214109.

138. J. Ren, Y. Wang, W. Li, T. Jiang, and Z. Shuai, "Time-Dependent Density Matrix Renormalization Group Coupled With n-Mode Representation Potentials for the Excited state Radiationless Decay Rate: Formalism and Application to Azulene," *Chinese Journal of Chemical Physics* 34, no. 5 (2021): 565–582.

139. Y. C. Wei, S. F. Wang, Y. Hu, et al., "Overcoming the Energy Gap Law in Near-Infrared OLEDs by Exciton–Vibration Decoupling," *Nature Photonics* 14, no. 9 (2020): 570–577.

140. A. Cravcenco, Y. Yu, F. Edhborg, et al., "Exciton Delocalization Counteracts the Energy Gap: A New Pathway Toward NIR-emissive Dyes," *Journal of the American Chemical Society* 143, no. 45 (2021): 19232–19239.

141. J. Zhao, Y. Gao, and R. Huang, et al., "Design of Near-Infrared-Triggered Metallo-photosensitizers via a Self-Assembly-Induced Vibronic Decoupling Strategy," *Journal of the American Chemical Society* 145, no. 21 (2023): 11633–11642.